Geoscience Frontiers 14 (2023) 101561

HOSTED BY

Contents lists available at ScienceDirect

Geoscience Frontiers

journal homepage: www.elsevier.com/locate/gsf

Research Paper

Early Cambrian high pressure/low temperature metamorphism in the southeastern Tarim craton in response to circum-Gondwana cold subduction

Qian Liu [a,*], Toshiaki Tsunogae [b,c], Guochun Zhao [d,a], Sam Uthup [b], Kazuki Takahashi [b], Jinlong Yao [a], Yu Wu [e], Yigui Han [a], Kei Ikehata [b]

[a] State Key Laboratory of Continental Dynamics, Department of Geology, Northwest University, Xi'an 710069, China
[b] Faculty of Life and Environmental Sciences, The University of Tsukuba, Ibaraki 305-8572, Japan
[c] Department of Geology, University of Johannesburg, Auckland Park 2006, South Africa
[d] Department of Earth Sciences, The University of Hong Kong, Pokfulam Road, Hong Kong, China
[e] Beijing Research Institute of Uranium Geology, Beijing 100029, China

ARTICLE INFO

Article history:
Received 21 June 2022
Revised 29 December 2022
Accepted 30 January 2023
Available online 2 February 2023
Handling Editor: Sanghoon Kwon

Keywords:
Early Paleozoic
High-pressure low temperature
Metamorphism
Cold subduction
Tarim craton
Gondwana

ABSTRACT

The circum-Gondwana subduction initiated by the early Cambrian has been suggested to reflect the establishment of the modern plate tectonics. The metamorphic rocks with low thermobaric (*T*/*P*) ratios indicative of cold subduction in the present tectonic regime have not been well investigated. To better understand the circum-Gondwana subduction and to test its possible link with the emergence of the modern plate tectonics, this study focused on blueschist-facies metamorphic rocks in the Altyn Tagh of the southeastern Tarim craton. Mineral assemblage and chemistry, phase equilibrium modelling, and quartz-in-garnet Raman elastic geobarometry reveal that the zoisite blueschist and glaucophane (Gln)-bearing quartz schist in northern Altyn Tagh were metamorphosed to lawsonite to epidote blueschist-facies at 520–545 °C and 16–19 kbar. It reflects high-pressure (HP)/low temperature (LT) metamorphism with low *T*/*P* ratios of <300 °C/GPa and thermal gradients of <10 °C/km. These blueschist-facies metamorphic rocks underwent rapid decompression starting at *P*-*T* conditions of <495 °C and <9.6 kbar during exhumation. Ar-Ar geochronology records paragonite Ar-Ar plateau ages of 520–506 Ma for the zoisite blueschist samples and phengite Ar-Ar plateau ages of 522–516 Ma for the Gln-bearing quartz schist samples, suggesting that the peak HP/LT metamorphism occurred prior to ca. 522 Ma. Based on new results and available data from the major Gondwana blocks, cold subduction was suggested to profoundly operate along circum-Gondwana in the early Cambrian after the amalgamation of Gondwana. The extensive circum-Gondwana subduction represents the earliest global cold subduction in Earth's history associated with the establishment of the modern plate tectonics, as directly recorded by the studied early Cambrian blueschist-facies metamorphic rocks and a dramatic drop in the mean *T*/*P* of metamorphism since the early Paleozoic.

1. Introduction

The initial subduction of the Proto-Tethys Ocean occurred along the northern margin of Gondwana in the early Cambrian (e.g., Yao et al., 2021), coincident with the subduction processes of the Iapetus Ocean and the Proto-Pacific Ocean along the western and southern margins of Gondwana, respectively (Murphy et al., 2006; Cawood and Buchan, 2007; Linnemann et al., 2008). Such circum-Gondwana subduction has been considered to reflect the establishment of the modern plate tectonic regime corresponding with global plate re-organization associated with the final assembly of Gondwana (Cawood and Buchan, 2007; Yao et al., 2021). Indicators for the circum-Gondwana subduction subject to the modern plate tectonics regime, which is characterized by sinking of cold, dense lithosphere at subduction zones, are primarily Mariana-type ophiolites and trench-arc assemblages (e.g., Yao et al., 2021). Unique metamorphic rocks, especially blueschist and low temperature (LT) eclogite as a hallmark of cold subduction with low geothermal gradients characterizing the present tectonic

* Corresponding author.
E-mail address: liuqian@nwu.edu.cn (Q. Liu).

https://doi.org/10.1016/j.gsf.2023.101561

regime (e.g., Brown and Johnson, 2018; Stern, 2018), have not been well investigated.

Blueschist and LT eclogite are generated under high pressure (HP)/LT conditions with low thermobaric (*T*/*P*) ratios and found only in the fluid-rich environments above the cold oceanic subduction zones (e.g., Tsujimori and Ernst, 2014; Stern, 2018), providing direct evidence of cold subduction. The early Paleozoic HP/LT metamorphic rocks are documented in the Altyn Tagh, the southeastern Tarim craton (Fig. 1), recording the initial subduction of the Proto-Tethys Ocean (Zhang et al., 2007). They are key to understanding the subduction processes along the margins of Gondwana and to testing the possible link between the circum-Gondwana subduction with the establishment of the modern plate tectonics. To date, only unprecise *P-T* conditions of 430–540 °C and 20–23 kbar based on conventional geothermobarometers have been obtained for eclogite in northern Altyn Tagh (Zhang et al., 2007), and the *P-T* conditions of blueschist in the region are unclear. Besides, an Ar-Ar plateau age of 512±3 Ma for phengite from eclogite and a younger Ar-Ar plateau age of 491±3 Ma for paragonite from blueschist have been reported and interpreted as the timing of peak eclogite-facies and late greenschist-facies metamorphism, respectively (Zhang et al., 2007). The age interpretations need further consideration, because the available peak metamorphic temperature (430–540 °C; Zhang et al., 2007) seemingly exceeds the closure temperature of Ar within white mica (350–400 °C; Purdy and Jager, 1976; Hames and Bowring, 1994).

P-T conditions are challenging to determine for blueschist-facies metamorphic rocks due to a lack of robust conventional geobarometers applicable to high pressure mineral parageneses (e.g., Li, 2020). Nonetheless, phase equilibrium modelling can provide significant information on metamorphic *P-T* conditions. Additionally, quartz-in-garnet geobarometry based on pressure-dependent Raman spectra of quartz inclusions has been applied to estimate pressure conditions at which they were trapped during garnet growth (e.g., Enami et al., 2007; Ashley et al., 2014; Yoneguchi et al., 2021). This study integrated petrography, mineral chemistry, phase equilibrium modelling, and quartz-in-garnet Raman elastic geobarometry to constrain the *P-T* evolution of the blueschist-facies metamorphic rocks in northern Altyn Tagh. Ar-Ar geochronology was also carried out to examine the timing of the HP/LT metamorphism in the region. New results define the subduction process of the Proto-Tethys Ocean in northern Gondwana. Combined with the subduction processes along the other margins of Gondwana, new insights were shed on the circum-Gondwana subduction that marks the oldest cold subduction globally in Earth's history.

2. Geological background

The Altyn Tagh is located along the southeastern margin of the Tarim craton, to the southwest of the Qilian orogen and the Qaidam block, and to the north of the East Kunlun orogen (Fig. 1a). The Altyn Tagh consists of four units, including the North Altyn Tagh terrane, the North Altyn Tagh subduction-accretion belt (NAT), the Central Altyn Tagh terrane, and the South Altyn Tagh subduction-collision belt (Fig. 1b).

Precambrian metamorphic rocks are dominated in the North Altyn Tagh terrane (Fig. 1c). Major lithologies are ca. 3.7 Ga and 2.8–2.5 Ga tonalite-trondhjemite-granodiorite gneiss, 2.0 Ga felsic and mafic gneiss, 1.9 Ga paragneiss, and 1.85 Ga granitic veins and mafic dykes (e.g., Ge et al., 2020 and references therein).

The NAT between the North Altyn Tagh terrane and the Central Altyn Tagh terrane has been considered as an early Paleozoic accretionary orogen (e.g., Zhang et al., 2015). It consists mainly of ca. 520–480 Ma supra-subduction zone (SSZ)-type ophiolitic mélanges (e.g., Liu et al., 2021a and references therein), 520–400 Ma magmatic rocks (summarized in Liu et al. 2021b), HP/LT blueschist and eclogite with white mica Ar-Ar isochron ages of 512–491 Ma (Zhang et al., 2007), and early Paleozoic volcanosedimentary rocks (Liu et al., 2021b). Some ca. 760–750 Ma mafic dykes and bimodal volcanic rocks have also been reported in the NAT (GSIX, 2009; Liu et al., 2012a; Li et al., 2020b).

The Central Altyn Tagh terrane preserves predominant Meso- to Neoproterozoic clastic and volcanic rocks, which are represented by weakly metamorphosed conglomerate, quartz sandstone,

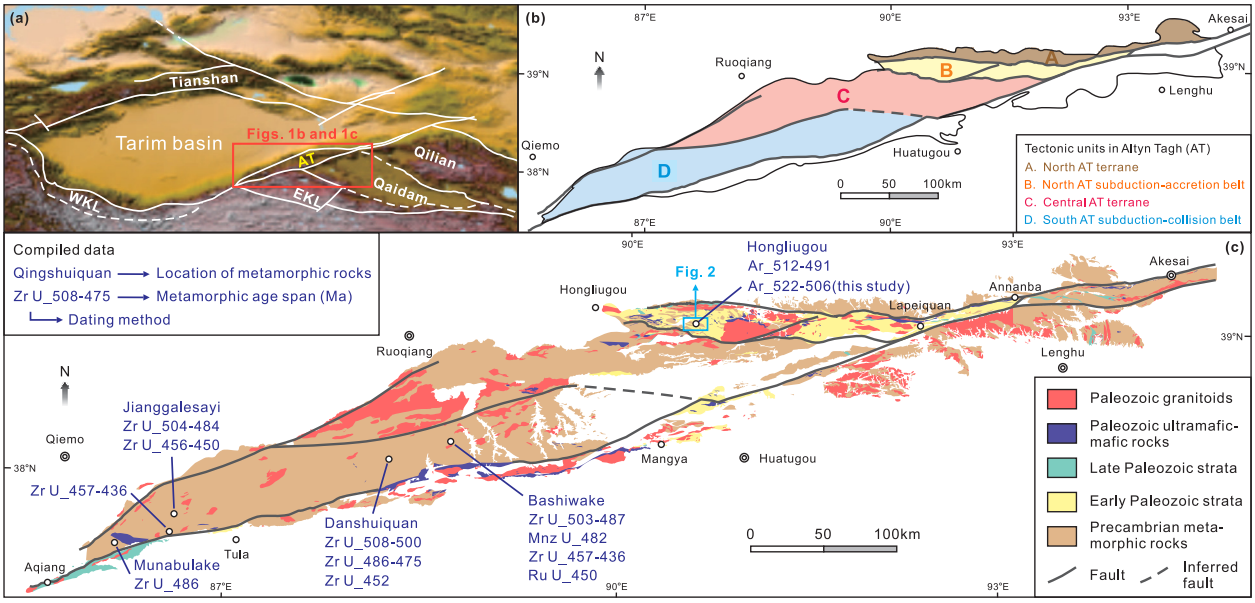

Fig. 1. (a) Topographic map (from website http://www.ngdc.noaa.gov/mgg/global/) showing location of the Altyn Tagh (AT) in the southeastern Tarim craton (modified from Lu et al., 2008). EKL— East Kunlun. (b) Simplified tectonic division of the Altyn Tagh (modified after Liu et al., 2012b; Wu, 2016). (c) Geological map of the Altyn Tagh (modified after GBGP, 1976; GBGP, 1977; GBGP, 1979; IGQP, 1984; IGQP, 1986; IGHP, 1985; RGGR, 2002; RGGR, 2003; RGHP, 2003; TIMR, 2007; XCGS, 2012) showing compiled ages of metamorphic rocks (Zhang et al., 2007, 2017; Liu et al., 2009, 2012b; Li et al., 2015, 2020c; Wang et al., 2016; Cao et al., 2019a, 2019b; Gai et al., 2022). Abbreviations for dating methods: Ar— Phengite/Paragonite $^{40}Ar/^{39}Ar$, Zr U— Zircon U-Pb, Ru U— Rutile U-Pb, and Mnz U— Monazite U-Pb.

volcanic layers, and limestone, in which maximum depositional ages of ca. 1.2 Ga were reported for quartzite (Gehrels et al., 2003). In addition, some ca. 522–433 Ma magmatic rocks and minor 920 Ma foliated rhyolite, 754 Ma basalt, and 703 Ma A-type granite are exposed in the terrane (GSIX, 2009; Zhang et al., 2010; Wang, 2011; Liu et al., 2016).

The South Altyn Tagh subduction-collision belt has been identified as an early Paleozoic collisional orogen (e.g., Zhang et al., 2015), as evidenced by ca. 508–475 Ma ultra(U)HP and ca. 457–436 Ma Barrovian-type metamorphic rocks (e.g., Liu et al., 2007, 2012b; Wang et al., 2016; Zhang et al., 2017) in the matrix of the Altyn Tagh Complex. The Altyn Tagh Complex consists mainly of Meso- to Neoproterozoic tonalitic-granodioritic gneiss and metasedimentary rocks (Wang et al., 2013; Yu et al., 2013). Ca. 501 Ma SSZ-type ophiolitic mélange (Li et al., 2009) and 504 Ma granite (Liu et al., 2016) are also recorded in the belt.

3. Field relation and sample description

The HP/LT metamorphic rocks occur as a tectonic sliver in the western segment of the NAT (Fig. 1c). They are in W–E striking reverse fault contact with the early Paleozoic volcanosedimentary sequences, which is cut by sinistral strike-slip fault relative to the Cenozoic Altyn Tagh fault system (Fig. 2). The HP/LT metamorphic rocks include zoisite blueschist, glaucophane (Gln)-bearing quartz schist, muscovite quartz schist, calcic muscovite schist, and quartzite (Fig. 3a). The zoisite blueschist is enclosed by (Fig. 3b) or intercalated with (Fig. 3c) the Gln-bearing quartz schist, both of which constitute a lens of a 2 m width (GPS: 39°07′0.47″N and 90°32′1.42″E) surrounded by muscovite quartz schist (Fig. 3a). In this study, three zoisite blueschist samples (19LQ03-9, −10, and −16) and four Gln-bearing quartz schist samples (19LQ03-4, −8–2, −22, and −24) were collected.

The zoisite blueschist samples show schistose structures defined by major elongated glaucophane and minor flaky paragonite (Fig. 4a – d). Garnet crystals are idiomorphic to subidiomorphic and show porphyroblastic and poikiloblastic textures (Fig. 4e and f). Zoisite, paragonite, titanite, chlorite, albite, and quartz are common inclusions in the inner domains of garnet (Fig. 4e and f), while zoisite, glaucophane, quartz, chlorite, and rutile are dominated in the outer domains of garnet (Fig. 4e and f). Zoisite commonly forms lath-like porphyroblasts with their long axes parallel to the foliation (Fig. 4b and c) and contains glaucophane, titanite, quartz, and chlorite inclusions (Fig. 4g and h). Occasionally, zoisite contains pumpellyite components in the central domains (Fig. 4h), suggesting prograde metamorphism from prehnite-pumpellyite- to blueschist-facies. Zoisite also occurs in the inner and outer domains of garnet (Fig. 4e and f). Glaucophane is tiny and elongated in shape and predominantly distributed in the matrix (Fig. 4a – c) with minor crystals as inclusions in zoisite and garnet (Fig. 4e – g). Paragonite is flaky in the matrix or inclusions in the garnet inner domains (Fig. 4d – f). Titanite is euhedral in the matrix or enclosed in the zoisite and garnet inner domains (Fig. 4g and h). Mineral relations coupled with geochemical components of garnet reflecting prograde metamorphism (details in the next section), the blueschist-facies mineral assemblage of garnet (outer domains) + glaucophane + zoisite + rutile + quartz + chlorite is recorded in the zoisite blueschist samples. Additionally, one omphacite crystal was identified in the garnet outer domains of sample 19LQ03-9 (Fig. 4f), implying that this sample had undergone eclogite-facies metamorphism but largely retrograded to epidote blueschist-facies. Retrogression is demonstrated by replacement of glaucophane by predominant winchite (Fig. 4i), which is locally replaced by magnesio-hornblende. Other evidence of retrograde metamorphism includes chloritization of garnet and zoisite (Fig. 4d), as well as chlorite, albite, and ferro-ferri-hornblende located in the fractures and edges of garnet (Fig. 4e and f).

The Gln-bearing quartz schist samples show schistosity with oriented phengite and elongated quartz (Fig. 5a – c). Garnet crystals are porphyroblastic and poikiloblastic with inclusions of zoisite, quartz, chlorite, and paragonite in the inner domains and rutile, quartz, chlorite in the outer domains (Fig. 5d). Some zoisite crystals are lath-like porphyroblasts with their long axes parallel to the foliation and contain phengite, titanite, quartz, and chlorite inclusions (Fig. 5a – c). Zoisite occasionally intergrows with

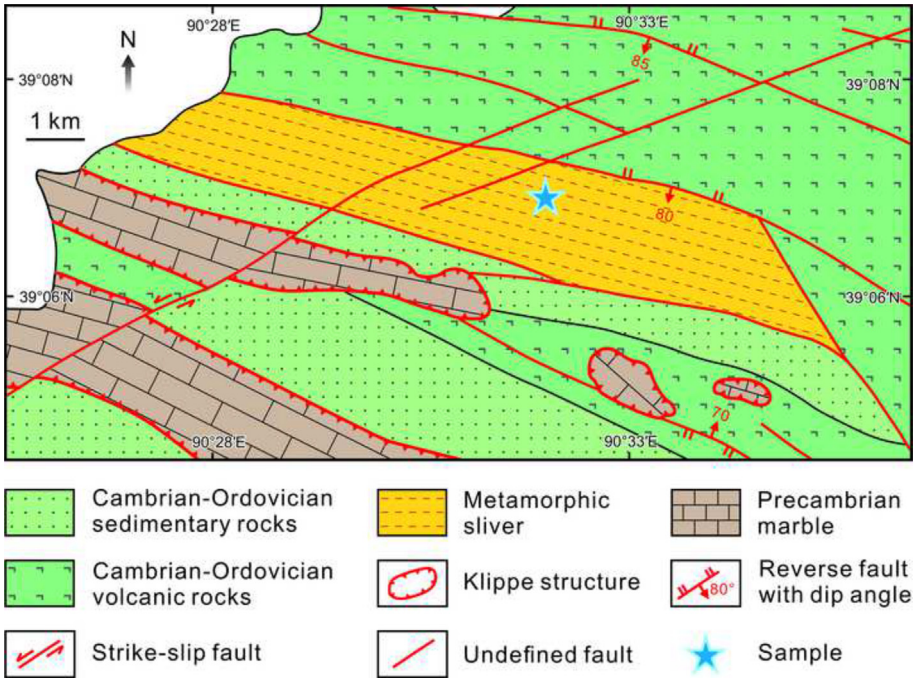

Fig. 2. Geological map showing sampling site in the western segment of the North Altyn Tagh subduction-accretion belt (modified after XCGS, 2012).

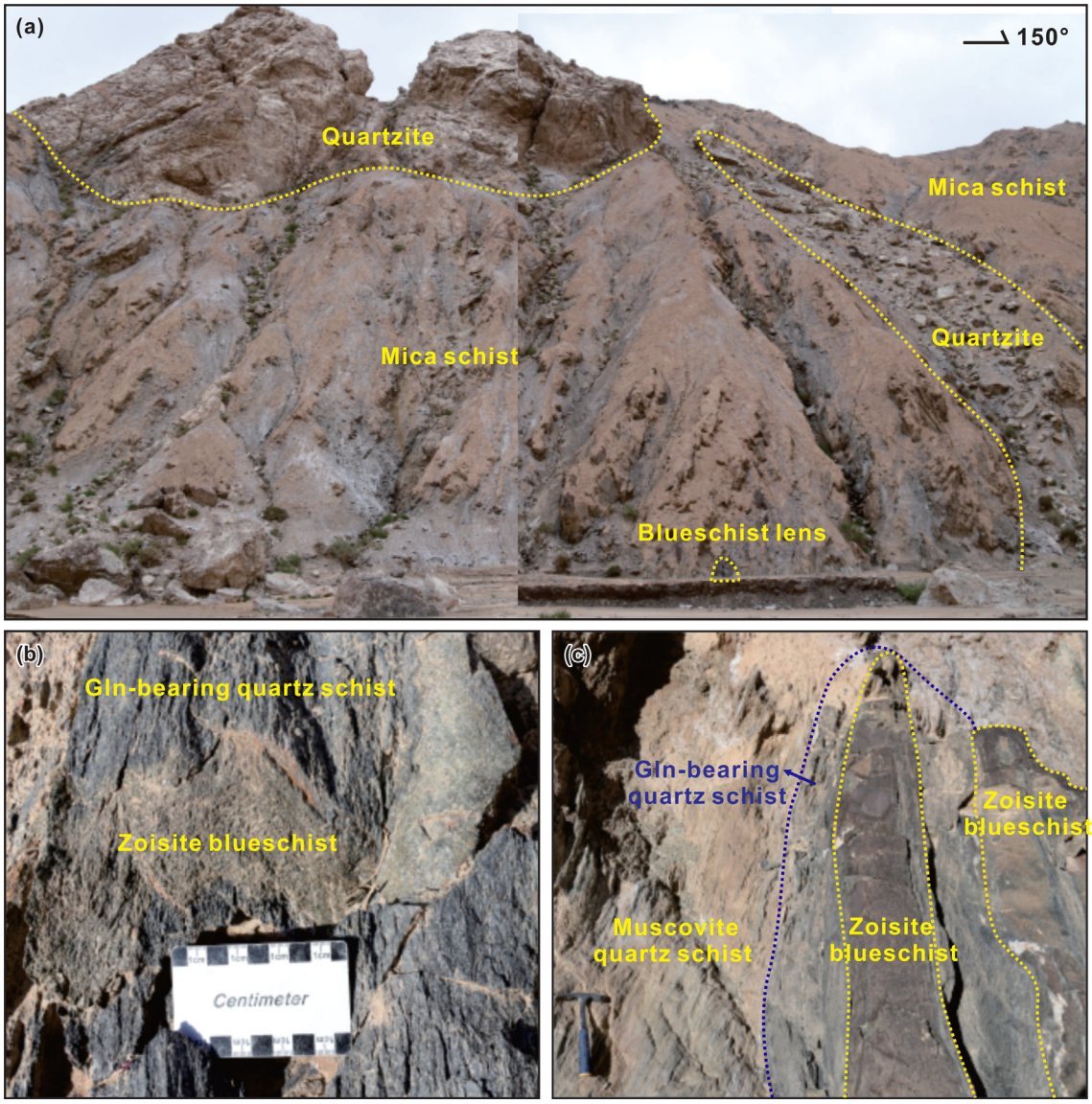

Fig. 3. Representative field photographs of (a) an overview of HP/LT metamorphic rocks, (b) zoisite blueschist enclosed by Gln-bearing quartz schist, and (c) zoisite blueschist intercalated with Gln-bearing quartz schist.

titanite + glaucophane + quartz ± phengite, which together preserves as lensoidal domains in the matrix (Fig. 5e – h). Glaucophane appears mainly in the matrix or as relics within zoisite (Fig. 5e – h). Locally, glaucophane shows chemical zoning (Fig. 5i) with more iron components in the outer domains. The matrix is composed mainly of quartz, phengite, and glaucophane. Albite is surrounded by matrix minerals (Fig. 5f), and chlorite is surrounded by garnet or occupies the fractures or retrograde domains of zoisite and garnet (Fig. 5c and d). Accordingly, the blueschist-facies mineral assemblage in the Gln-bearing quartz schist samples is garnet + phengite + glaucophane + zoisite + rutile + quartz + chlorite.

4. Analytical methods

A wavelength-dispersive spectroscopy electron microprobe (JEOL JXA8530F Hyperprobe) was applied for mineral chemical analysis at the Chemical Analysis Division of the Research Facility Center for Science and Technology, the University of Tsukuba, Japan. Accelerating voltage, beam current, and focal spot diameter were set at 15 kV, 10nA, and 3 μm, respectively. For raw data correction, an oxide-ZAF correction method was adopted. The mineral chemical data is presented in Supplementary Data Table S1.

Whole-rock major-element compositions were analyzed by using a Thermo Scientific ARL 9900 X-ray fluorescence (XRF) spectrometer at FocuMS Technology Co., Ltd., Nanjing, China. For quality control, BHVO-2 and AGV-2 (U.S. Geological Survey rock reference materials) were used, and uncertainties were <2%. FeO/Fe_2O_3 ratio was determined by titration. The whole-rock major-element data is listed in Supplementary Data Table S2.

Phase equilibrium modelling was conducted for samples 19LQ03-10 and 19LQ03-16 by employing THERMOCALC 3.47 with a thermodynamic dataset of tc-ds62 (Powell and Holland, 1988; Holland and Powell, 1998; Holland and Powell, 2011; Green et al., 2016). Pseudosection modelling was undertaken in the system of Na_2O-CaO-K_2O-FeO-MgO-Al_2O_3-SiO_2-H_2O-TiO_2-Fe_2O_3 (NCKFMASHTO; Holland and Powell, 2011; Green et al., 2016), which is the most suitable approximation for the studied blueschist samples. In the modeling, MnO was ignored because of its

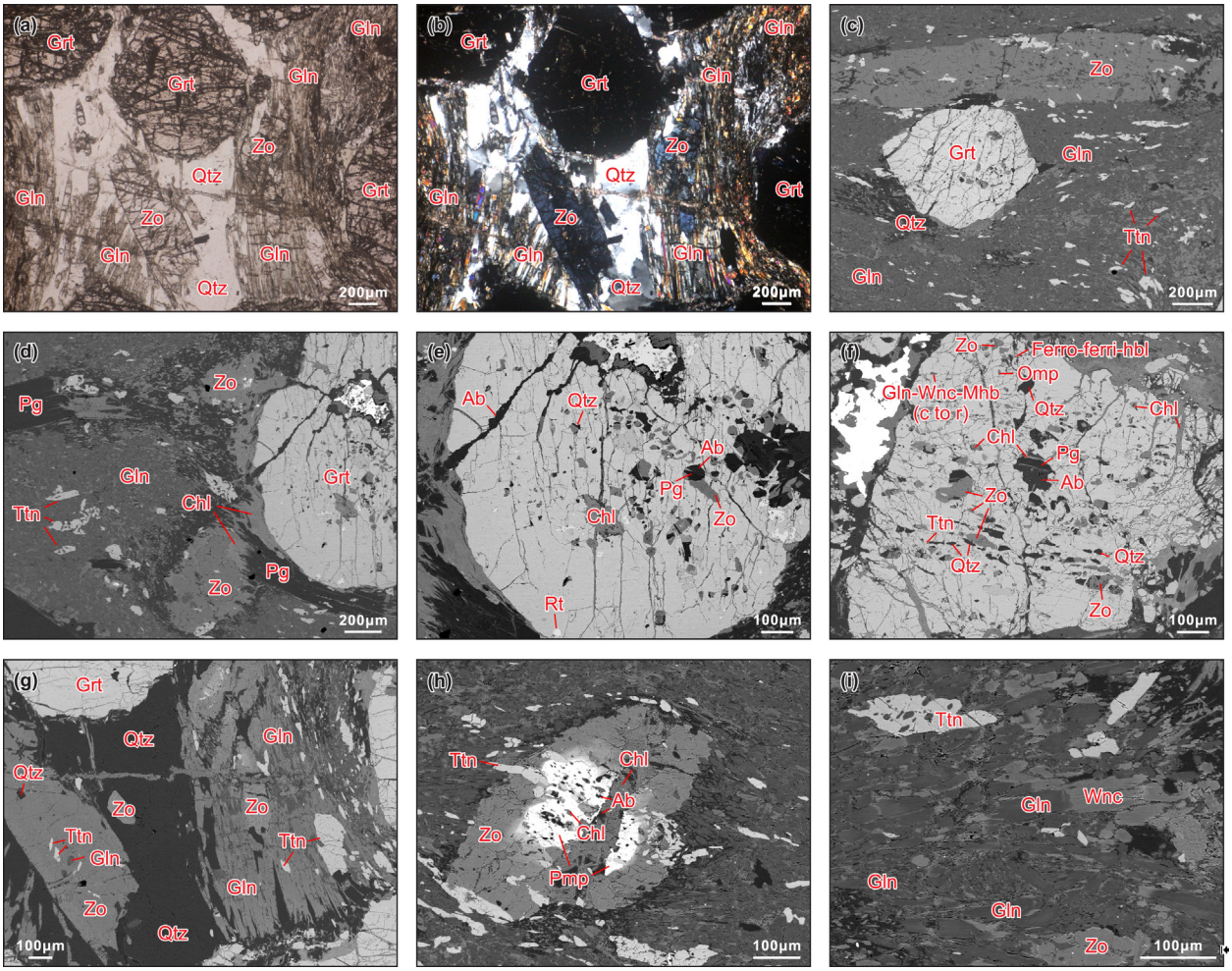

Fig. 4. (a–c) Representative photomicrographs and (d–i) backscattered (BSE) images of zoisite blueschist samples. Descriptions are detailed in the text. (a) and (b) are the photomicrographs of sample 19LQ03-10 from the same vision under plane and crossed polarization, respectively. Mineral abbreviations: Zo— Zoisite, Qtz— Quartz, Grt— Garnet, Gln-Glaucophane, Ttn— Titanite, Pg— Paragonite, Chl— Chlorite, Ab— Albite, Rt— Rutile, Omp— Omphacite, Wnc— Winchite, Mhb— Magnesio-hornblende, Ferro-ferri-hbl— Ferro-ferri-hornblende, and Pmp— Pumpellyite.

low content (<0.3 wt.%), and water content was set to excess. The applied phases in the modelling and their corresponding activity composition models were garnet and chlorite (White et al., 2014), clinoamphibole (Green et al., 2016), epidote (Holland and Powell, 2011), plagioclase (Holland and Powell, 2003), and ilmenite (White et al., 2000). Quartz, rutile, titanite, albite, lawsonite, and H_2O were fixed as pure phases.

The Raman spectra of quartz in garnet from samples 19LQ03-10 and 19LQ03-4 were obtained at Faculty of Life and Environmental Sciences, the University of Tsukuba, Japan. A Renishaw inVia Raman microscope is equipped with an 1800 lines/mm grating To obtain ambient peak positions, we used Herkimer quartz standard. 1 μm spot diameter of 532 nm excitation laser and approximate 20 mW irradiation power on the sample surface were applied. Spectra were acquired for 5–30 s and 5 s for the inclusions and standard, respectively. For spectral accuracy, before and after the inclusion measurements, the quartz standard was analyzed. Each quartz inclusion was analyzed twice with mostly <2% uncertainties and the average value was used for calculation and plotting. A microscope (100x, N.A. = 0.85) was equipped to centralize the laser. A silicon wafer's 520.5 cm^{-1} band was calibrated to 520.5±0.1 cm^{-1} for the spectrometer. A spectral resolution of 4 cm^{-1} was used, and the spectra were analyzed at conditions of atmospheric pressure and room temperature. To fit the quartz peaks, the raw data was primarily obtained based on the vicinity of 464, 205, and 127 cm^{-1} peaks of quartz and PeakFit v4.12, followed by applying a linear baseline subtraction and a PearsonIV model (Schmidt and Ziemann, 2000). The quartz inclusion pressure was calculated based on strains via stRAinMAN (Angel et al., 2019). The quartz phonon-mode Grüneisen tensors were referred to Murri et al. (2019). The obtained strains were transformed to a mean stress according to a matrix relationship (Nye, 1957) and quartz elastic moduli (Wang et al., 2015). The entrapment pressure of quartz was calculated by using EoSFit-Pinc with an elastic model of Angel et al. (2017b). A full *P-T-V* equation of state by Angel et al. (2017a) was calculated for quartz volumes, and an advanced Tait *P-T-V* equation of state by Holland and Powell (2011) was applied for garnet volumes. Wang and Ji (2001)'s shear moduli were used for garnet end members. The used garnet outer domain components were $Alm_{65}Prp_8Grs_{26}Sps_1$ and $Alm_{65}Pyr_7Gr_{27}Sps_{0.5}$ for a blueschist sample 19LQ03-10 and a Gln-bearing quartz schist sample 19LQ03-4, respectively. The Raman analytical results are presented in Supplementary Data Table S3.

Paragonite and phengite for Ar-Ar geochronology were separated by applying heavy liquid and magnetic separation techniques. Paragonite and phengite separates were irradiated for 24 h at Northwest Institute of Nuclear Technology, Xi'an, China.

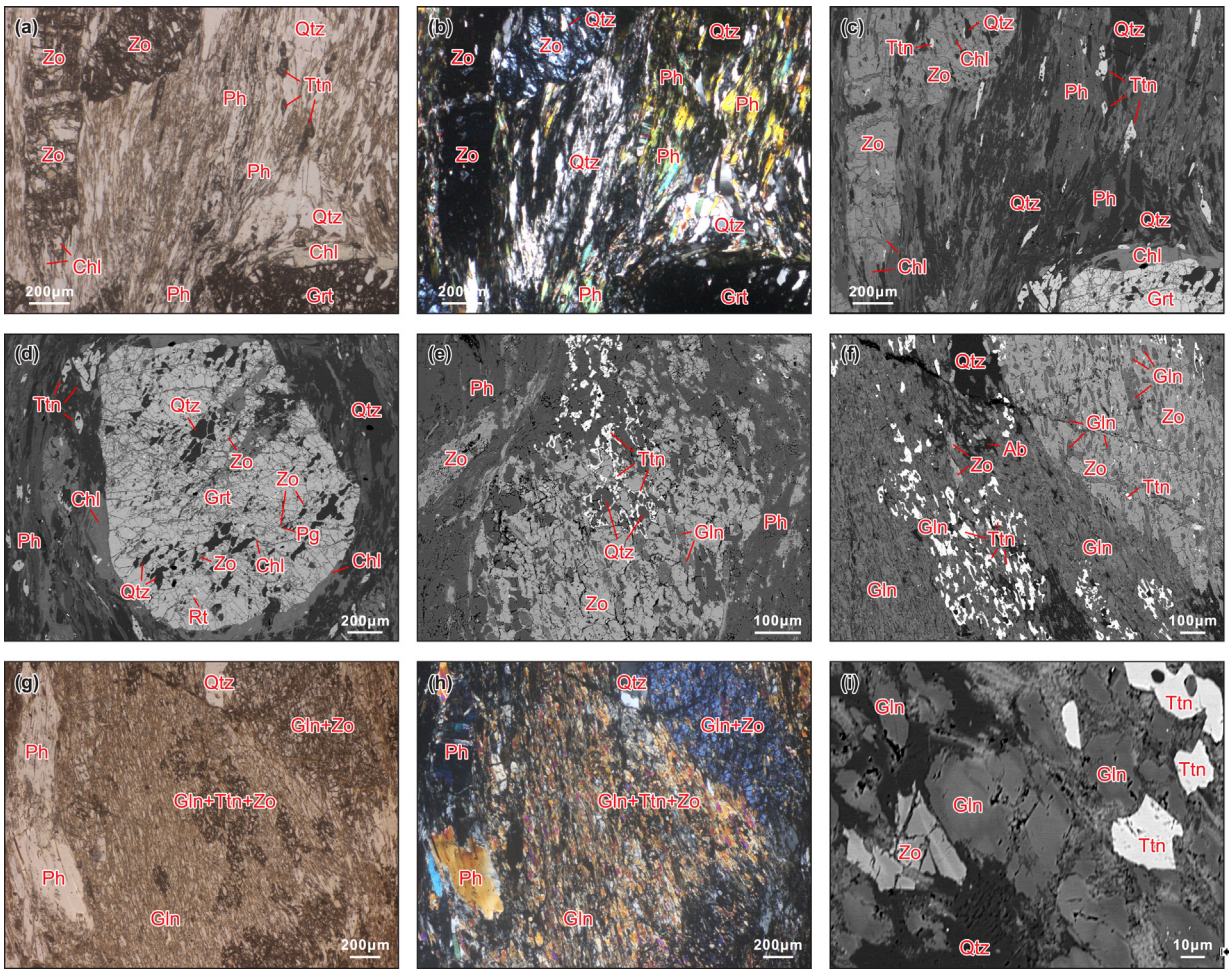

Fig. 5. (a–b and g–h) Representative photomicrographs and (c–f and i) backscattered (BSE) images of Gln-bearing quartz schist samples. Descriptions are detailed in the text. (a), (b), and (c) are from the same vision of sample 19LQ03-22; (g) and (h) are from the same vision of sample 19LQ03-24. Ph— Phengite, and other mineral abbreviations are the same as Fig. 4.

The national standard ZBH-25 (biotite) with an age of 132.7±1.2 Ma and the standard GBW04418 (amphibole) with an age of 2060±8 Ma were used to monitor neutron fluxes. Ar isotopes of the irradiated minerals were measured by using noble gas mass spectrometry Helix SFT at the Analytical Laboratory, Beijing Research Institute of Uranium Geology, China. Step-heating was performed at 9–11 steps with incrementally elevated power. All primary data was corrected, according to the obtained correction factors of interfering Ar isotopes during the irradiation in this study: $(^{36}Ar/^{37}Ar)_{Ca}$ = 0.0003011, $(^{39}Ar/^{37}Ar_o)_{Ca}$ = 0.0007694, and $(^{40}Ar/^{39}Ar)_K$ = 0.0020826. ^{37}Ar was corrected for radiogenic decay, and the applied decay constant of ^{40}K is $\lambda = 5.543\times10^{-10}$ a^{-1} (Steiger and Jäger, 1977). The Ar isotopic results are shown in Supplementary Data Table S4.

5. Results

5.1. Mineral chemistry

5.1.1. Garnet

Garnet crystals in all the studied samples are comparably almandine-rich, with components of $Alm_{59-69}Prp_{4-10}Grs_{21-31}Sps_{0.3-9}$ and $Alm_{59-69}Pyr_{5-9}Grs_{21-29}Sps_{2-6}$ in the zoisite blueschist and Gln-bearing quartz schist samples, respectively. Garnet displays weak zoning from inner to outer domain with decreases in spessartine and almandine components and increases in grossular and pyrope components, reflecting prograde growth (Fig. 6).

5.1.2. Amphibole

Based on nomenclature of amphiboles by (Leake et al., 1997) and method for calculating amphibole formula by (Li et al., 2020a), predominant amphibole minerals in the studied samples are classified as glaucophane (Fig. 7). Regardless of occurring as inclusions in garnet and zoisite or as matrix compositions, glaucophane crystals have Si contents of 7.56–7.99 p.f.u. and Na_B contents of >1.51 p.f.u. (Fig. 7) with $Mg/(Mg + Fe^{2+})$ ratios of 0.51–0.71. Winchite occupying the outer domains of glaucophane shows various Si contents of 6.86–7.71 p.f.u., Na_B contents of 0.50–1.18 p.f.u., and $Mg/(Mg + Fe^{2+})$ ratios of 0.58–0.76. Winchite is locally replaced by magnesio-hornblende with low Na_B contents of 0.39–0.45 p.f.u. and high $Mg/(Mg + Fe^{2+})$ ratios of 0.72–0.75 (Fig. 7). One ferro-ferri-hornblende inclusion occurs in the edge of one garnet crystal shows low Na_B contents of 0.20–0.30 p.f.u. and $Mg/(Mg + Fe^{2+})$ ratios of 0.43–0.47 (Fig. 7).

5.1.3. Zoisite

Assuming all iron to be Fe^{3+} (e.g., Armbruster et al., 2006), zoisite inclusions in garnet and zoisite associated with garnet contain high Fe^{3+} contents of 0.22–0.73 p.f.u. Comparatively, zoisite in the matrix shows various Fe^{3+} contents of 0.08–0.38 p.f.u., and no obvi-

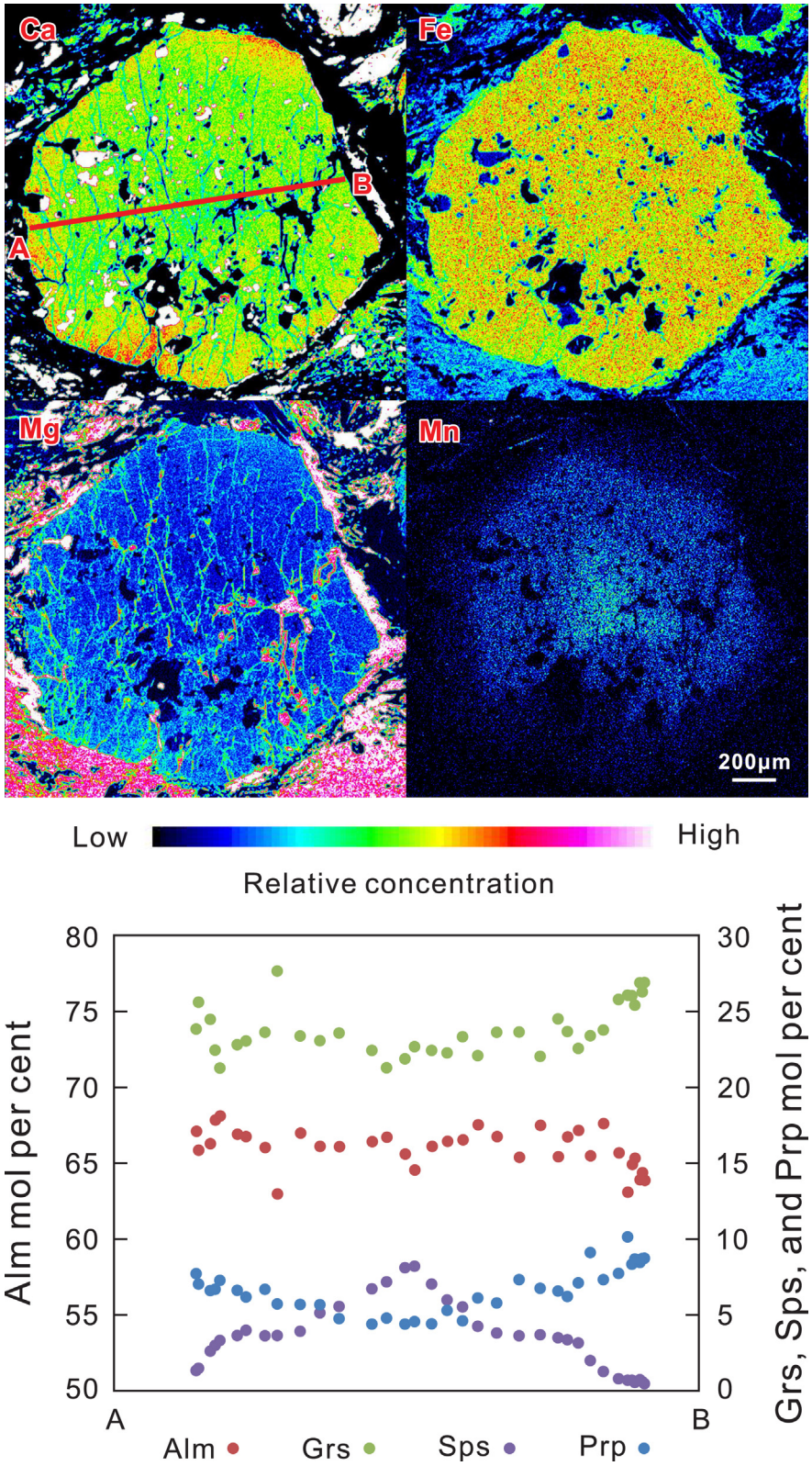

Fig. 6. Compositional mapping and profiles of almandine (Alm), grossular (Grs), spessartine (Sps), and pyrope (Prp) components of a representative garnet crystal from sample 19LQ03-16.

ous zoning was detected for a single zoisite crystal. Zoisite in sample 19LQ03-24 intergrowing with titanite + quartz + glaucophane ± phengite contains relatively high Fe^{3+} contents of 0.22–0.40 p.f.u.

5.1.4. Other minerals

One omphacite inclusion in garnet from sample 19LQ03-9 has Mg/(Mg + Fe^{2+}) ratios of 0.53–0.57, Na/(Ca + Na) ratios of 0.44–0.48, and Al contents of 0.34–0.42p.f.u. Paragonite shows concen-

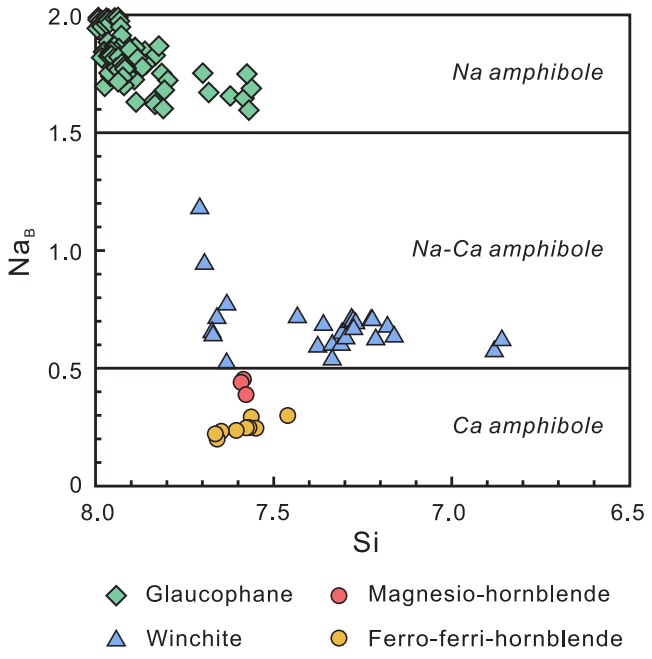

Fig. 7. Si (p.f.u.) versus Na_B (p.f.u.) diagram showing compositions of amphibole (after Leake et al., 1997).

trated Si contents of 5.91–6.25 p.f.u. based on 22 oxygen calculation and high Na/(Na + K) ratios of 0.83–0.99 with no obvious difference between paragonite in the matrix and garnet. Phengite in the Gln-bearing quartz schist samples has Si and Mg + Fe contents of 6.58–7.07 p.f.u. and 0.84–1.27 p.f.u., respectively, based on 22 oxygen calculation. Feldspar is pure albite (An mostly <5) and titanite is slightly aluminous (Al = 0.04–0.16 p.f.u.) in the studied samples.

5.2. Whole-rock major-element compositions

The zoisite blueschist samples have low SiO_2 contents of 49.2–50.1 wt.%, and high FeO (11.3–12.3 wt.%), MgO (5.79–5.95 wt.%), CaO (5.27–7.60 wt.%), and NaO (2.58–2.82 wt.%) contents. Comparatively, the Gln-bearing quartz schist samples have higher SiO_2 (58.7–65.9 wt.%) with lower FeO (2.80–7.75 wt.%), MgO (2.70–4.72 wt.%), CaO (2.66–3.97 wt.%), and NaO (1.47–1.76 wt.%) contents. In the Niggli index discrimination diagram (Fig. 8a), all studied samples plot into the field of sedimentary rocks, reflecting sedimentary protoliths (Winkler, 1976). According to sedimentary source discrimination (Roser and Korsch, 1988), the protoliths of the zoisite blueschist samples were probably derived from mafic igneous provenance (Fig. 8b), as also supported by their large amounts of glaucophane and zoisite. The protoliths of the Gln-bearing quartz schist samples show quartzose sedimentary provenance (Fig. 8b), consistent with abundant garnet, phengite, and quartz components in these samples.

5.3. P-T estimation

5.3.1. Phase equilibrium modelling

Figs. 9 and 10 illustrate *P-T* pseudosections calculated for the zoisite blueschist samples 19LQ03-10 and 19LQ03-16, respectively. Peak metamorphic mineral assemblage is represented by garnet (outer domain) + glaucophane + epidote (zoisite) + rutile + chlorite + quartz, with a wide *P-T* range of 510–580 °C and 13–19 kbar (Figs. 9 and 10).

For sample 19LQ03-10, the lawsonite-out line limits the upper-pressure stability, while the hornblende-in line constrains the lower-pressure stability (Fig. 9). Its upper- and lower-temperature stabilities are defined by the chlorite-out and titanite-out lines, respectively (Fig. 9). The peak metamorphic *P-T* condition of sample 19LQ03-10 was further constrained by using X_{Alm} isopleths of garnet outer domains (average of 0.86–0.87) to 520–547 °C and 15.0–18.5 kbar (Fig. 9). The retrograde metamorphic *P-T* condition at 480–496 °C and 8.6–9.5 kbar was estimated based on the stability of hornblende + epidote (zoisite) + titanite + chlorite + albite + quartz + paragonite (Fig. 9).

Similar lawsonite-out and hornblende-in lines limit the pressure stabilities for sample 19LQ03-16 (Fig. 10). The chlorite-out line defines the upper-temperature stability of sample 19LQ03-16, and its lower-temperature stability is constrained by the garnet-in line (Fig. 10). X_{Alm} isopleths of garnet outer domains

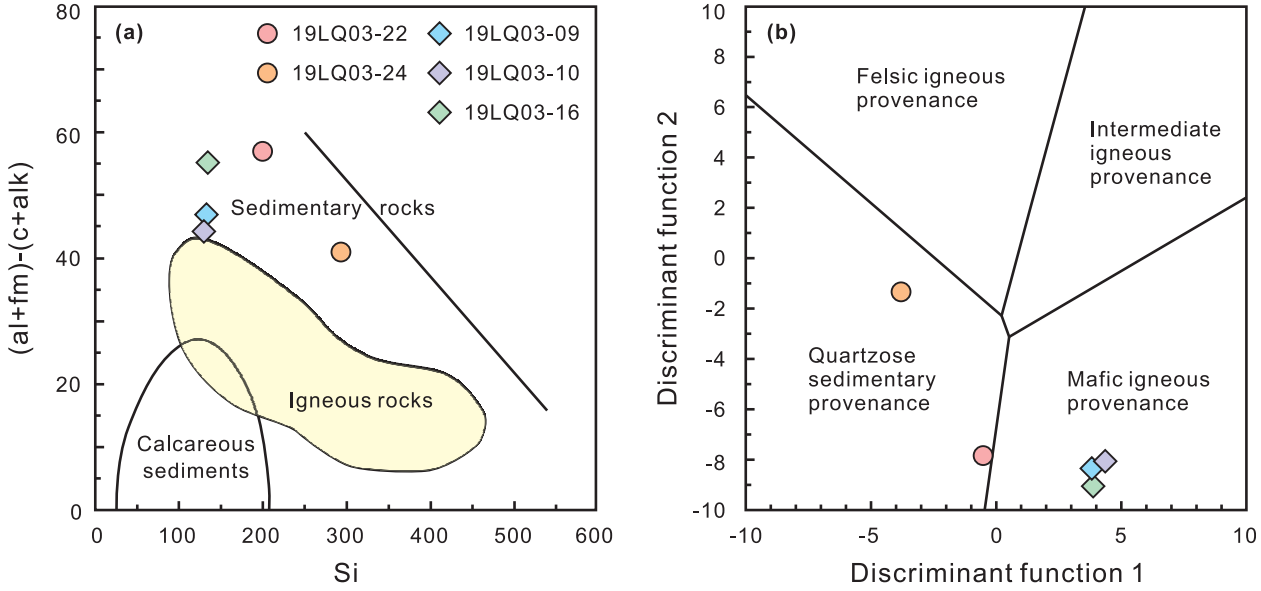

Fig. 8. (a) Niggli index discrimination diagram (after Winkler, 1976) and (b) sedimentary source discrimination diagram (after Roser and Korsch, 1988) of the studied metamorphic rocks.

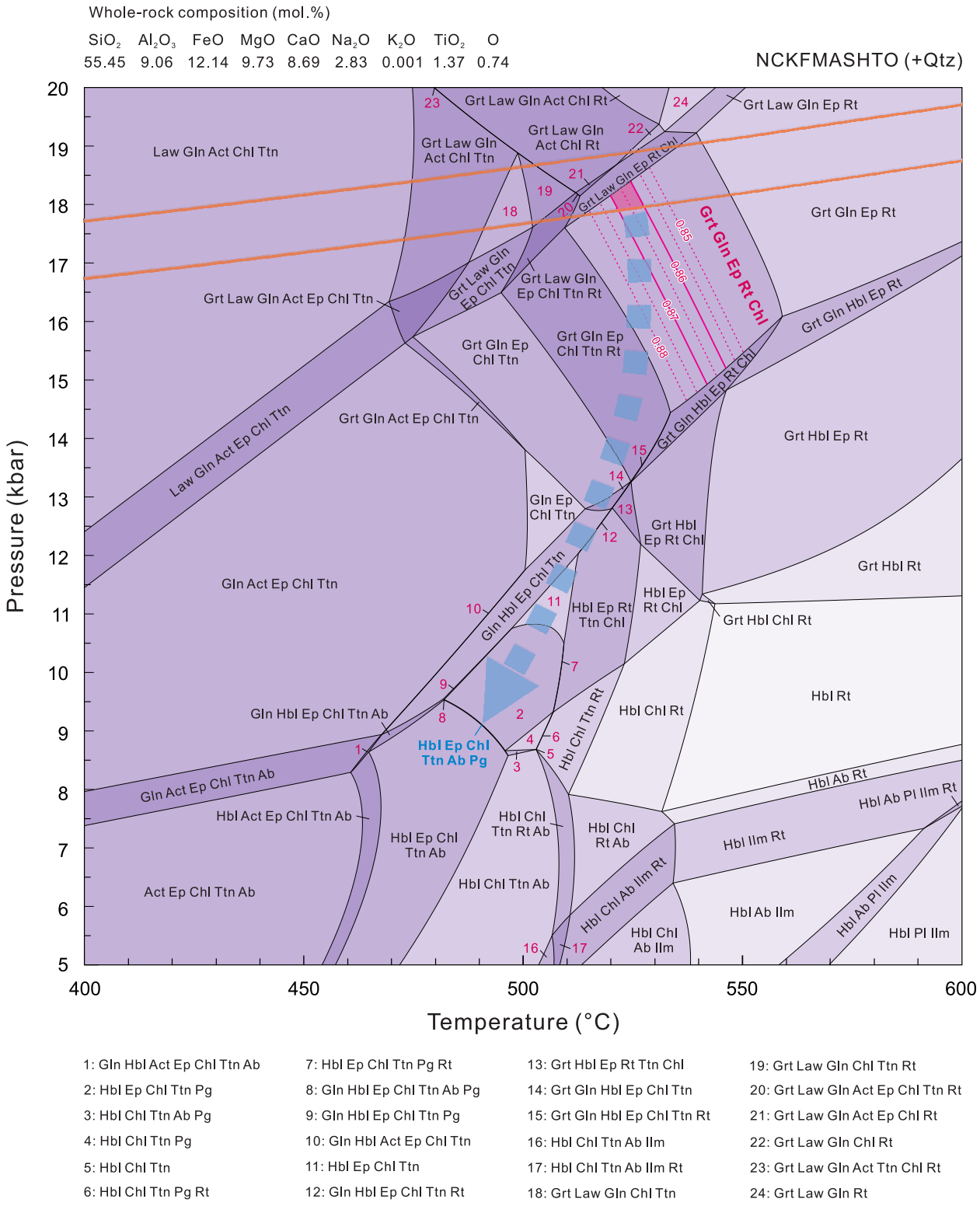

Fig. 9. *P-T* diagram showing calculated pseudosection of the mineral assemblage in the zoisite blueschist sample 19LQ03-10 in the NCKFMASHTO system. Orange lines are the calculated entrapment isomekes based on quartz-in-garnet Raman elastic geobarometry, and pseudosection was contoured with isopleths of almandine contents in garnet. The estimated field of peak *P-T* condition is filled with red, and dashed arrow marks the inferred *P-T* path of sample 19LQ03-10. Mineral abbreviations are from Whitney and Evans (2010).

(average of 0.85–0.86) and X_{Fe} isopleths of glaucophane (average of 0.34–0.36) further constrain the peak metamorphic *P-T* condition at 530–546 °C and 15.8–17.2 kbar for sample 19LQ03-16 (Fig. 10). The retrogression was defined by hornblende + epidote (zoisite) + titanite + chlorite + albite + quartz at <495 °C and <9.6 kbar (Fig. 10).

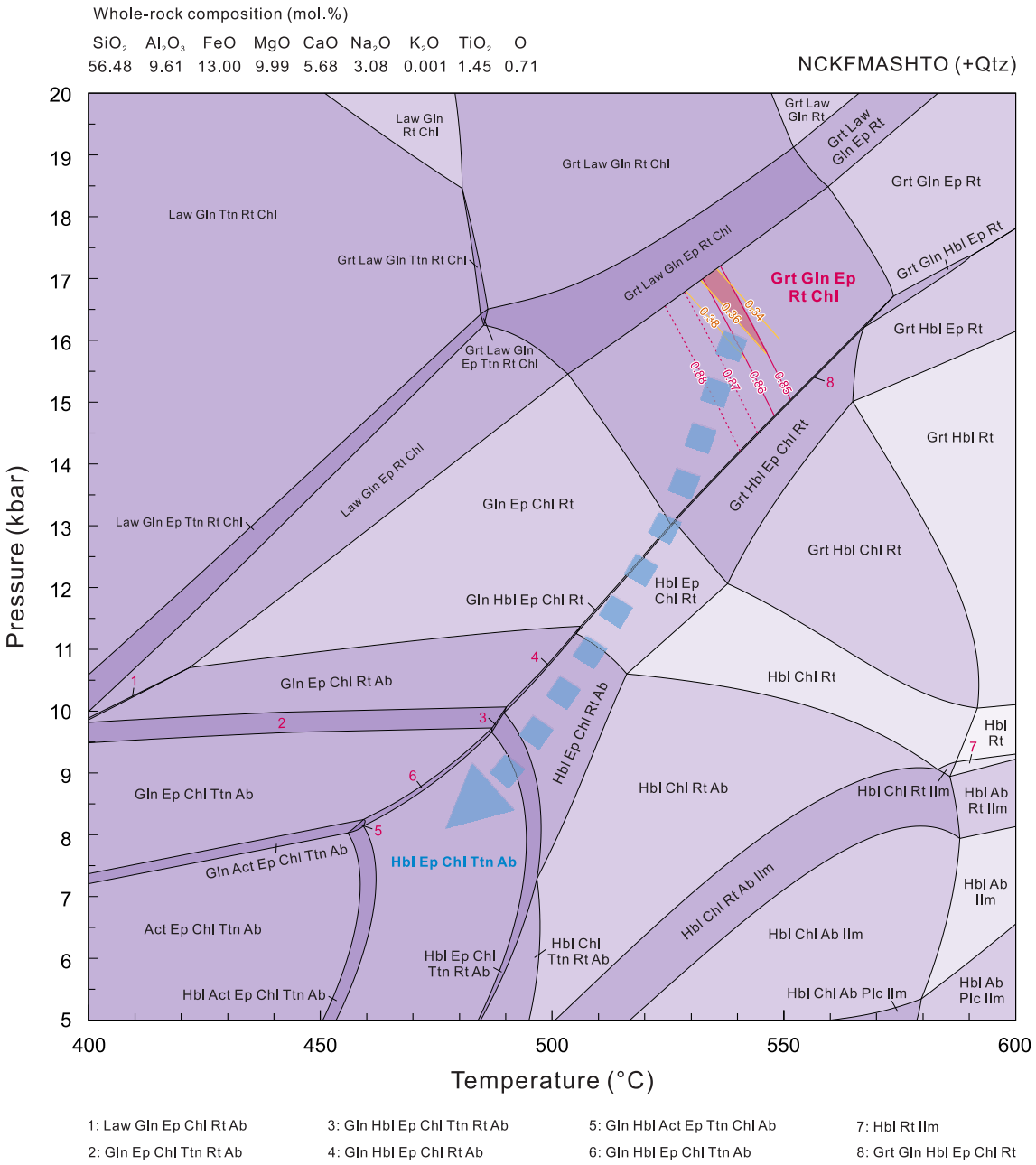

Fig. 10. P-T diagram showing calculated pseudosection of the mineral assemblage in the zoisite blueschist sample 19LQ03-16 in the NCKFMASHTO system. The pseudosection was contoured with isopleths of almandine contents in garnet (red) and iron contents in glaucophane (yellow). The estimated field of peak P-T condition is filled with red, and dashed arrow suggests the P-T path of sample 19LQ03-16. Mineral abbreviations are from Whitney and Evans (2010).

5.3.2. Quartz-in-garnet Raman elastic geobarometry

Raman elastic geobarometry on quartz inclusions trapped in the garnet outer domains in the zoisite blueschist sample 19LQ03-10 records entrapment pressures of 17.9–18.9 kbar (at 525 °C; Fig. 11). The Gln-bearing quartz schist sample 19LQ03-4 has a large range of calculated inclusion pressures, varying from 14.4 to 18.0 kbar (an average of 16.5 kbar) at 525 °C (Fig. 11). Correlation between the location of quartz inclusion in garnet and the calculated entrapment isomeke is challenging to observe in sample 19LQ03-4.

5.4. Ar-Ar geochronology

Paragonite extracted from the zoisite blueschist sample 19LQ03-9 recorded a plateau age of 520±2 Ma (mean square of weighted deviate (MSWD) = 1.6; Fig. 12a) covering 55% of the total released ^{39}Ar. This plateau age is in concordance with an isochron age of 514±7 Ma (MSWD = 1.7) yielding a near-atmospheric initial ^{40}Ar/^{36}Ar value of 317±24 (Fig. 12b). Paragonite from the blueschist sample 19LQ03-16 yielded a plateau age of 506±3 Ma (MSWD = 7.2; Fig. 12c), which was constrained by 83% ^{39}Ar released. A consistent isochron age of 501±7 Ma (MSWD = 7.6) was obtained with a near-atmospheric initial ^{40}Ar/^{36}Ar value of 317±26 (Fig. 12d).

Phengite from the Gln-bearing quartz schist sample 19LQ03-8–2 gave a plateau age of 522±2 Ma (MSWD = 2.1; Fig. 12e), defined by more than 97% released ^{39}Ar. An equal isochron age of 522±2 Ma (MSWD = 2.2) with a near-atmospheric initial ^{40}Ar/^{36}Ar value of 268±32 was obtained for phengite from sample 19LQ03-8–2 (Fig. 12f). Phengite from the Gln-bearing quartz schist sample 19LQ03-22 yielded a plateau age of 516±2 Ma (MSWD = 1.8;

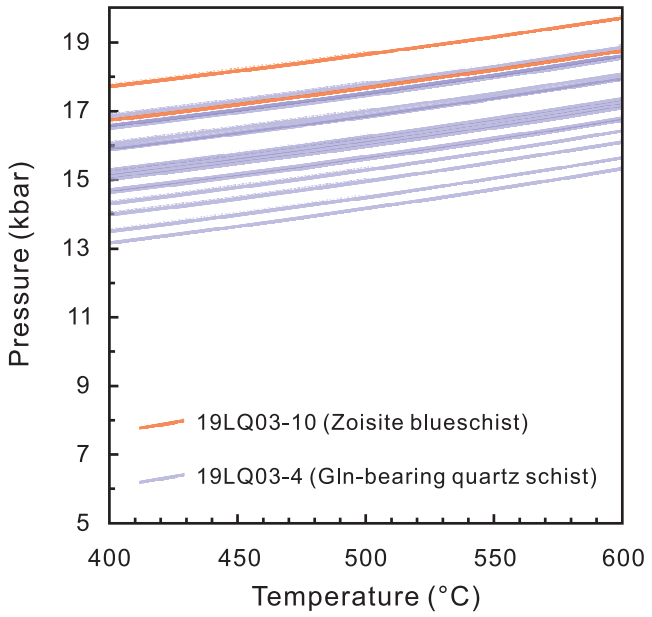

Fig. 11. *P-T* diagram presenting the calculated entrapment isomekes based on quartz-in-garnet Raman elastic geobarometry.

Fig. 12g) and a similar isochron age of 515±3 Ma (MSWD = 2.0; Fig. 12h). These ages were calculated based on more than 95% released ^{39}Ar and produced a near-atmospheric initial $^{40}Ar/^{36}Ar$ value of 308±29.

6. Discussion

6.1. P-T evolution

The peak metamorphic *P-T* range of the zoisite blueschist sample 19LQ03-10 was primarily defined by pseudosection calculation based on the stability of peak mineral assemblage (garnet outer domain + glaucophane + zoisite + rutile + chlorite + quartz) and X_{Alm} isopleths of garnet outer domains (Fig. 9). This *P-T* range intersects the calculated entrapment isomeke deduced from Raman elastic geobarometry on the quartz inclusions in the garnet outer domains, which potentially records the maximum pressure condition because of the prograde growth of garnet in the sample, as indicated by mineral chemistry (Fig. 6). Accordingly, we estimated a peak metamorphic *P-T* condition at 520–528 °C and 17.8–18.5 kbar for sample 19LQ03-10 (Fig. 9). Another zoisite blueschist sample 19LQ03-16 yielded a consistent peak metamorphic *P-T* range of 530–546 °C and 15.8–17.2 kbar defined by the calculated pseudosections and isopleths of garnet X_{Alm} and glaucophane X_{Fe} (Fig. 10). The Gln-bearing quartz schist samples were probably equilibrium at the same metamorphic conditions with the zoisite blueschist samples, as evidenced by their close association in the outcrop (Fig. 3b and c) and the same peak mineral assemblage of garnet (outer domain) + glaucophane + epidote (zoisite) + rutile + chlorite + quartz. This suggestion is also supported by the calculated quartz inclusion pressures up to 18.0 kbar at 525 °C for a Gln-bearing quartz schist sample 19LQ03-4 (Fig. 11).

Notably, the quartz-in-garnet entrapment isomeke of the zoisite blueschist sample 19LQ03-10 suggests a possible maximum pressure condition up to 19 kbar (at 525 °C, Fig. 9), which falls into the pressure range of lawsonite blueschist-facies metamorphism. The intergrowth of glaucophane and zoisite in the Gln-bearing quartz schist samples (Fig. 5f – h) with oxidized bulk compositions probably records the following reaction, indicative of the entry from lawsonite to epidote blueschist-facies (i.e., Evans, 1990; Ao and Bhowmik, 2014).

$$Omp + Lws \rightarrow Gln + Ep + Qtz + H_2O$$

Collectively, the studied samples experienced lawsonite to epidote blueschist-facies metamorphism at 520–545 °C and 16–19 kbar with low *T*/*P* ratios (<300 °C/GPa) and corresponding thermal gradients of <10 °C/km (Brown and Johnson, 2018). It reflects HP/LT metamorphism, in agreement with the coeval eclogite adjacent to the sampling location with conventional geothermobarometers yielding peak *P-T* conditions of 430–540 °C and 20–23 kbar (Zhang et al., 2007) and comparable $Alm_{62-70}Prp_{6-10}Grs_{23-27}Sps_{1-6}$ components of garnet (Zhang et al., 2007).

Retrograde metamorphism of the studied blueschist-facies metamorphic rocks was indicated by the stability of the mineral paragenesis of hornblende + epidote (zoisite) + titanite + chlorite + albite + quartz ± paragonite (Figs. 9 and 10). The retrograde *P-T* condition of 480–496 °C and 8.6–9.5 kbar was estimated by the pseudosection calculation for the zoisite blueschist sample 19LQ03-10 (Fig. 9), comparable with the rapid retrogression *P-T* condition of <495 °C and <9.6 kbar for the zoisite blueschist sample 19LQ03-16 (Fig. 10). According to the above *P-T* estimations, the blueschist-facies metamorphic rocks probably underwent fast decompression due to exhumation (Figs. 9 and 10).

6.2. Timing of HP/LT metamorphism

The zoisite blueschist samples 19LQ03-9 and 19LQ03-16 yielded paragonite Ar-Ar plateau ages of 520–506 Ma (Fig. 12a and b), and phengite from the Gln-bearing quartz schist samples 19LQ03-8–2 and 19LQ03-22 gave Ar-Ar plateau ages of 522–516 Ma (Fig. 12c-d). Previous study reported a similar Ar-Ar plateau age of ca. 512 Ma for phengite from eclogite and a younger Ar-Ar plateau age of ca. 491 Ma for paragonite from blueschist (Zhang et al., 2007). Generally, the closure temperature of Ar within white mica are well documented at ca. 350–400 °C (Purdy and Jager, 1976; Hames and Bowring, 1994). The Ar-Ar ages of 522–506 Ma recorded in the studied blueschist-facies metamorphic rocks and reported eclogite (Zhang et al., 2007) probably reflect the retrograde metamorphism during exhumation stage after peak blueschist-facies metamorphism. A younger Ar-Ar plateau age of 491±3 Ma for paragonite from blueschist has also been reported by Zhang et al. (2007). Paragonite in that blueschist sample is closely associated with the edge of glaucophane with orientation intersecting with schistosity, implying the late crystallization of paragonite (Zhang et al., 2007). Accordingly, the younger paragonite Ar-Ar age of 491 Ma was interpreted as the timing of late greenschist-facies metamorphism (Zhang et al., 2007). Considering the oldest Ar-Ar plateau age of 522 Ma obtained in this study and the *P-T* evolution of the zoisite blueschist samples demonstrating fast decompression at exhumation stage (Figs. 9 and 10), we inferred that the peak HP/LT metamorphism might have occurred in the early Cambrian (prior to ca. 522 Ma).

6.3. Cold subduction along circum-Gondwana initiated by the early Cambrian

In this study, the early Cambrian HP/LT blueschist-facies metamorphic rocks from northern Altyn Tagh suggest that the subduction of the Proto-Tethys Ocean had commenced before ca. 522 Ma along the southeastern Tarim craton. This suggestion is also supported by ca. 521 Ma Qingyazi SSZ-type ophiolite in northern Altyn Tagh (Zhang et al., 2009), ca. 518 Ma Munabulake Mariana-type ophiolite in southern Altyn Tagh (Yao et al., 2021), and ca. 515 Ma oldest arc-related magmatic rocks in Altyn Tagh (e.g., Han et al., 2012; Meng et al., 2017). The subduction initiation of

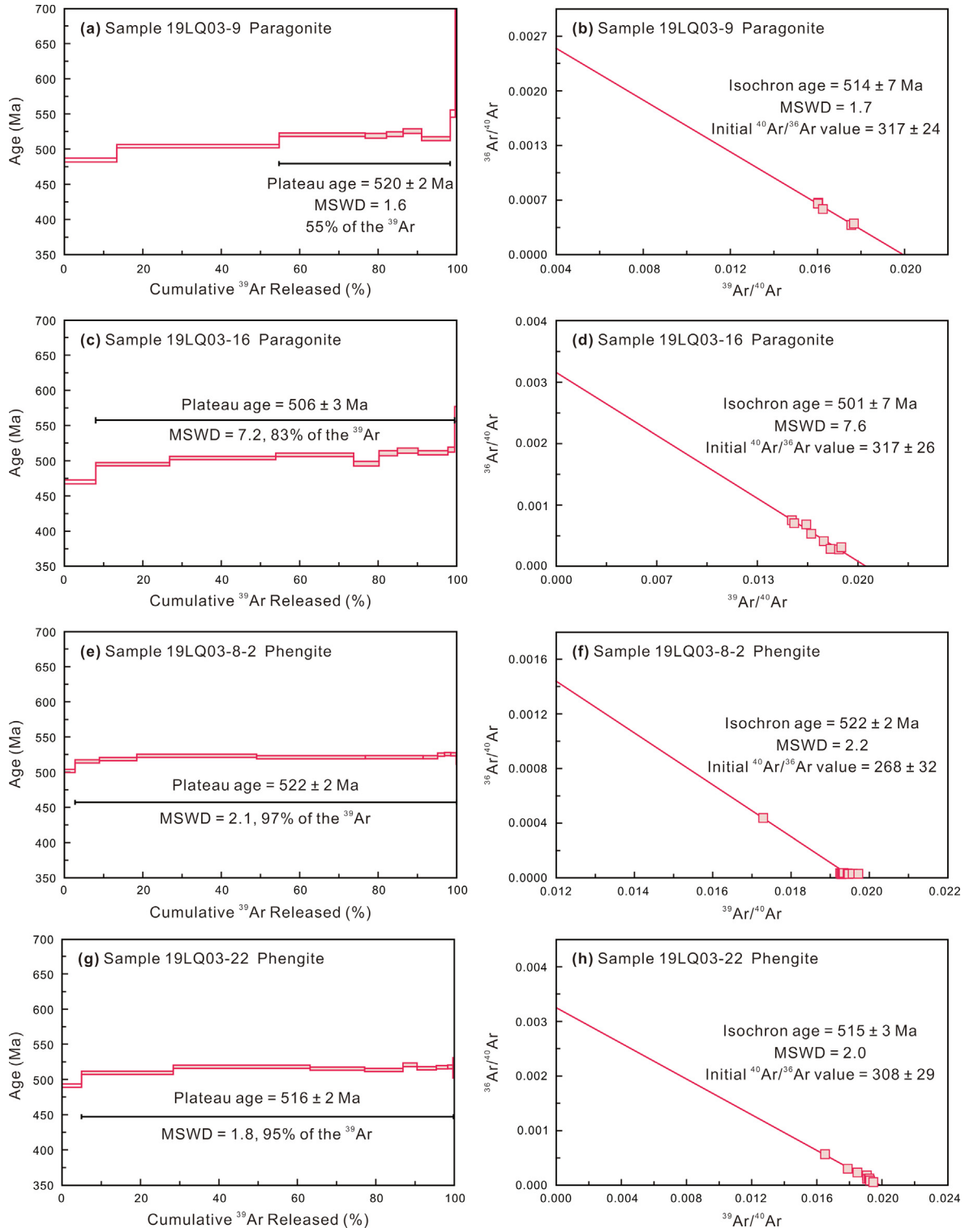

Fig. 12. $^{40}Ar/^{39}Ar$ apparent age spectra and corresponding inverse isochron plots of (a-b) paragonite from the zoisite blueschist sample 19LQ03-9, (c-d) paragonite from the zoisite blueschist sample 19LQ03-16, (e-f) phengite from Gln-bearing quartz schist sample 19LQ03-8–2, and (g-h) phengite from Gln-bearing quartz schist sample 19LQ03-22.

the Proto-Tethys Ocean is also sporadically recorded in some East Asian continental blocks along the northern margin of Gondwana (e.g., Li et al., 2018; Zhao et al., 2018). For example, ca. 533–513 Ma oldest arc-related magmatism (Yin et al., 2020) and ca. 516–512 Ma Kudi back-arc ophiolite in West Kunlun (Wang et al., 2021) indicate the subduction initiation of the Proto-Tethys Ocean should have occurred prior to ca. 533 Ma in West Kunlun. The Proto-Tethys Ocean had existed in East Kunlun since the late Sinian, as suggested by ca. 555 Ma oceanic island basalt (OIB)-type Kuhai ophiolite (Li et al., 2007). Its subduction in East Kunlun probably had commenced in the early Cambrian based on the recognition of ca. 537–520 Ma SSZ-type ophiolites

(Wei, 2015; Qi et al., 2016) and 550–490 Ma subduction-related granitic magmatism and metamorphism (Dong et al., 2018 and reference therein). The North Qilian region crops out ca. 525 Ma ophiolite and ca. 517–505 Ma tholeiite magmatic rocks in response to early-stage subduction (Xia et al., 2012; Song et al., 2013), recording the subduction initiation of the Proto-Tethys Ocean since ca. 525 Ma in North Qilian. The ophiolitic assemblages with middle-ocean ridge basalt (MORB) affinities in North Qinling indicate the formation of the Proto-Tethys Ocean between the North and South China blocks at ca. 534–517 Ma, and the subduction occurred at ca. 515 Ma producing predominant arc-related gabbroic and granitic intrusions (summarized in Dong et al., 2011; Dong and Santosh, 2016). Along the northern margin of India, Tethyan Himalaya and Amdo underwent convergent Andean-type margin activity in response to the subduction of the Proto-Tethys Ocean at 560–530 Ma (Cawood et al., 2007, 2021; Guynn et al., 2012). Collectively, the initial subduction of the Proto-Tethys Ocean started at ca. 535–515 Ma along the northern margin of Gondwana, constituting the North Indo-Australie Orogen (Fig. 13). With respect to the subduction initiation along the other Gondwana's margins, the timing is relatively earlier. The subduction initiation of the Proto-Pacific Ocean operating eastern Australia, southern Antarctica, and western South America along the southern margin of Gondwana, i.e. the Terra Australis Orogen (Fig. 13), probably occurred as earlier as ca. 590–560 Ma (e.g., Cawood and Buchan, 2007; Schwartz et al., 2008; Hagen-Peter et al., 2016). In addition, as a part of the Avalonian-Cadomian Orogen in the margin of West Gondwana (Fig. 13), the accretionary orogen due to the subduction of the Iapetus Ocean commenced at ca. 600 Ma at the periphery of West Africa and the Iranian Block (Linnemann et al., 2008; Moghadam et al., 2021). Therefore, the overall timing of the oceanic subduction initiation along circum-Gondwana was diachronous, commencing at ca. 590–560 Ma along the southern and western margins and ca. 535–515 Ma in the northern margin.

Yao et al. (2021) considered the intense subduction initiation along circum-Gondwana accomplished by the early Cambrian marking the establishment of modern plate tectonic regime during that time, primarily evidenced by Mariana-type ophiolites and trench-arc assemblages. Nonetheless, the HP/LT metamorphism, directly indicative of cold subduction in the modern tectonic regime, is worthy to be considered regarding circum-Gondwana subduction processes. This study identified early Cambrian (slightly prior to ca. 522 Ma) HP/LT blueschist-facies metamorphism with low T/P ratios of <300 °C/GPa and thermal gradients of <10 °C/km in northern Altyn Tagh, providing a direct record of the cold subduction processes of the Proto-Tethys Ocean in northern Gondwana.

Despite that other coeval blueschist-facies metamorphic rocks have not yet been reported in northern Gondwana, the available

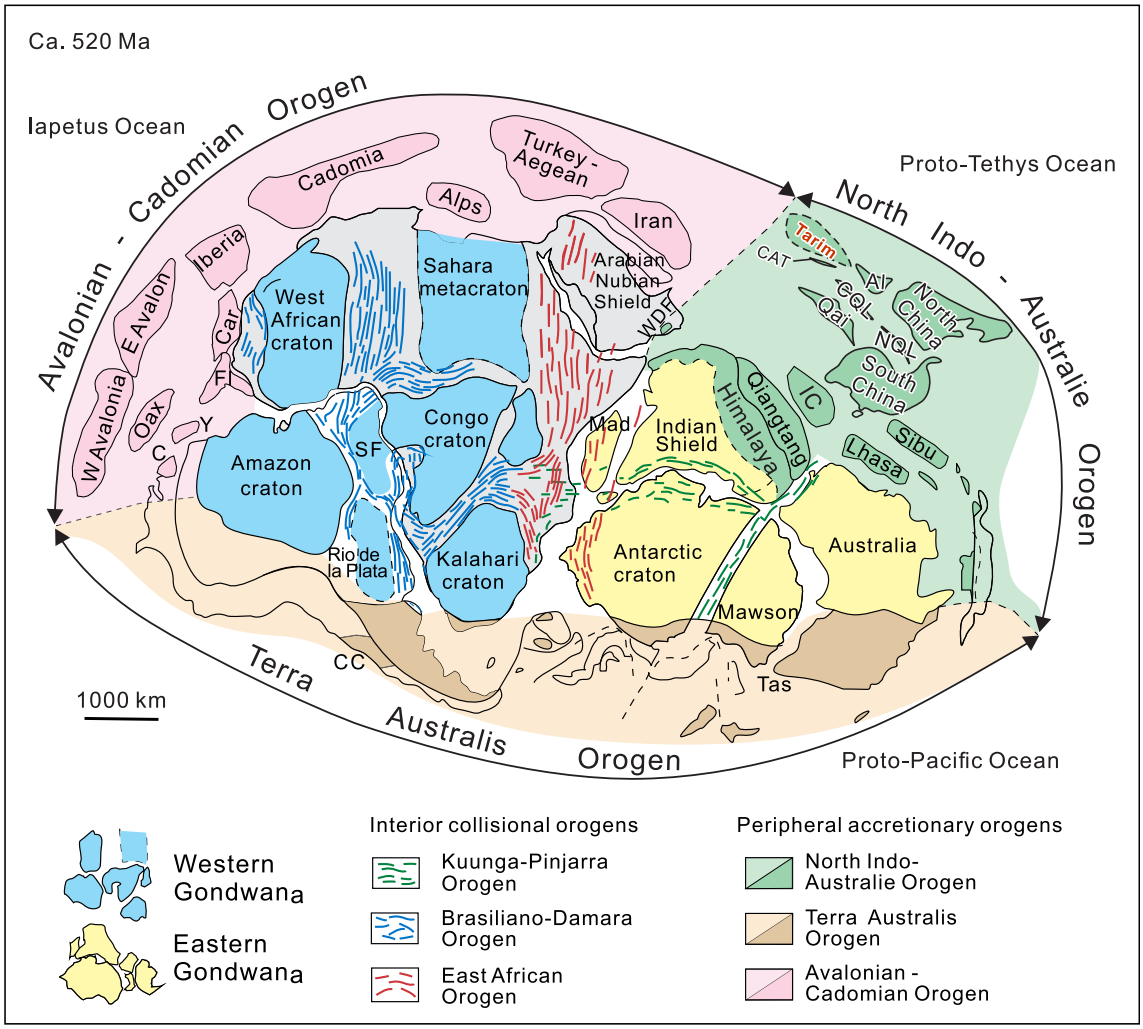

Fig. 13. Reconstruction of Gondwana at ca. 520 Ma (modified after Cawood et al., 2021; Liu et al., 2021b). Abbreviations: CAT— Central Altyn Tagh, AL— Alxa, CQL— Central Qilian, Qai— Qaidam, NOL— North Qinling, IC— Indochina, Sibu— Sibumasu, WDF— Western Deformational Front, Oax— Oaxaquia, C— Cortis, Y— Yucatan, Fl— Florida, Car— Carolina, CC— Cuyania and Chilenia, SF— San Francisco, Mad— Madagascar, and Tas— Tasmania.

subduction-related metamorphic records in the East Asian blocks also support the cold subduction processes of the Proto-Tethys Ocean. For example, in North Qilian, a low-grade blueschist belt and a high-grade blueschist belt containing massive blocks of eclogite were identified to be a cold subduction zone with low thermal gradients of ~6 – 7 °C/km (Song et al., 2013 and reference therein). The timing of the peak HP/LT metamorphism in North Qilian was constrained to be 490–460 Ma (Song et al., 2013; Cheng et al., 2016), slightly younger than that in northern Altyn Tagh. Some orthogneiss and amphibolite in East Kunlun contain a number of metamorphic zircons with a large range U-Pb age of 549–517 Ma (Chen et al., 2008), interpreted as the timing of the subduction-related metamorphism (Dong et al., 2018). Subduction-related metamorphic rocks are also documented in North Qinling, represented by (U)HP eclogite metamorphosed at ca. 516–486 Ma under 2.2–3.1 GPa and 550–770 °C conditions (Wang et al., 2011; Cheng et al., 2012; Dong and Santosh, 2016) and garnet amphibolite yielding peak metamorphic ages of 515 Ma and *P-T* conditions of 15–19 kbar and 750–850 °C (Tang et al., 2016). The cold subduction conditions with ~10 °C/km thermal gradients can be inferred in North Qinling accordingly. The early Paleozoic high-grade metamorphism might have also been preserved in Himalaya to the north of India, as implied by various metamorphic ages of 550–435 Ma (Cawood et al., 2007). In addition, ca. 530–500 Ma UHP eclogite with peak metamorphic conditions up to 800–850 °C and 23–25 kbar was reported in East Antarctica and southeastern Australia along the southern margin of Gondwana (Palmeri et al., 2009; Romer et al., 2009; Di Vincenzo et al., 2016), even though coeval HP/LT blueschist-facies metamorphism is lacking. Collectively, cold subduction was profoundly operative along the margins of Gondwana in the early Cambrian (Fig. 13), which is directly recorded by the early Cambrian blueschist-facies metamorphic rocks in the northern Altyn Tagh.

6.4. Implications for the earliest global, cold subduction in Earth's history

Brown and Johnson (2018) distinguished three types of metamorphism based on *T*/*P* ratios. They are high *T*/*P* type (*T*/*P* >775 °C/GPa) represented by common and ultra-high temperature granulite, intermediate *T*/*P* type (*T*/*P* of 375–775 °C/GPa) including HP granulite and middle- to high-temperature eclogite, and low *T*/*P* type (*T*/*P* <375 °C/GPa) dominated by blueschist, LT eclogite, and UHP metamorphic rocks (Fig. 14). With minor exceptions, the low *T*/*P* metamorphic rocks were absent in Earth's history until the late Neoproterozoic (Fig. 14), in which blueschist and LT eclogite are generally associated with cold subduction in accretionary orogens and UHP metamorphic rocks normally occur in collisional orogens (e.g., Brown and Johnson, 2019). The emergence of the low *T*/*P* metamorphism in the late Neoproterozoic was attributed to the secular cooling of mantle (Holder et al., 2019) facilitating deep breakoff of subducting slab and deep subduction of continental lithosphere (Sizova et al., 2014; Brown et al., 2020). However, whether the cold subduction and collision orogens operated globally in the late Neoproterozoic remains ambiguous. The first evidence of blueschist-facies metamorphism is ca. 800–750 Ma Aksu blueschist in northwestern Tarim (Yong et al., 2013; Xia et al., 2019). Precambrian blueschist-facies metamorphic records are scarce, as only exemplified by ca. 560–550 Ma blueschist in the Anglesey-Lleyn accretionary orogen in UK (Kawai et al., 2007) and blueschist of uncertainly Pan-African ages in West Africa (Caby et al., 2008). Major evidence of Precambrian low *T*/*P* metamorphism is UHP eclogite with peak metamorphic ages of 650–600 Ma limited within the West Gondwana-forming orogens, including the Pan-African orogenic system in western and southern Africa (John and Schenk, 2003; Liégeois et al., 2003; Reno et al., 2012; Berger et al., 2014) and the collisional orogen between South America and West Africa (Reno et al., 2012; Ganade de Araujoet al., 2014).

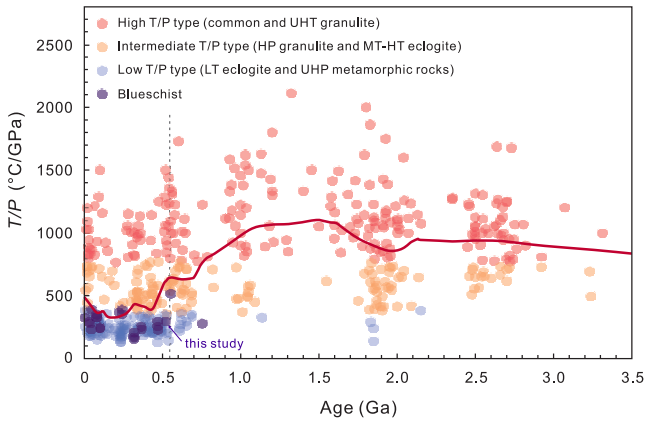

Fig. 14. Metamorphic thermobaric ratios (*T*/*P*) for three types of metamorphic rocks plotted against age (Data from Brown and Johnson, 2019 and this study) and locally weighted scatter plot smoothing (LOWESS) curve (after Brown et al., 2020). Dashed line represents the boundary between the Precambrian and the Phanerozoic. UHT— ultrahigh temperature, HP— high pressure, MT— middle temperature, HT— high temperature, LT— low temperature, and UHP— ultrahigh pressure.

Alternatively, the early Cambrian subduction along circum-Gondwana (Fig. 13) registers a globally linked network of narrow plate boundaries, probably representing the earliest cold subduction of a global behavior in Earth's history. Such global, cold subduction is coincident with the widespread occurrence of blueschist and a dramatic drop in the mean *T*/*P* of metamorphism in the earliest Paleozoic (Fig. 14), interpreted to mark the establishment of the modern plate tectonic regime (Yao et al., 2021). The interval of the late Neoproterozoic to early Paleozoic might have been the transitional period of a change to the global, cold subduction and the establishment of the modern plate tectonics. This period coincides well with the amalgamation of Gondwana at ca. 670–500 Ma (e.g., Cawood and Buchan, 2007; Schmitt et al., 2018). The resultant mountain building and subsequent erosion contributed to high sediment fluxes as lubrication for convergent plate interfaces, which intensified subduction facilitating sustained plate tectonics (Sobolev and Brown, 2019). This scenario is also indicated by remarkably evolved Hf-O isotopic compositions of ca. 720–540 Ma zircons due to considerable crustal reworking during the amalgamation of Gondwana (Gardiner et al., 2016). In the early Cambrian, the circum-Gondwana subduction accomplished after the amalgamation of the main Gondwana blocks (Fig. 13) (e.g., Cawood et al., 2007; Yao et al., 2021), marking the earliest cold subduction globally in Earth's history indicative of the emergence of the modern plate tectonics.

7. Conclusion

The zoisite blueschist and Gln-bearing quartz schist in the Altyn Tagh southeastern Tarim, experienced HP/LT lawsonite to epidote blueschist-facies metamorphism at 520–545 °C and 16–19 kbar with low *T*/*P* ratios of <300 °C/GPa and thermal gradients of <10 °C/km. They underwent fast decompression under *P-T* condition of <495 °C and <9.6 kbar during exhumation. The peak HP/LT metamorphism probably occurred in the early Cambrian, slightly prior to ca. 522 Ma. The early Cambrian blueschist-facies metamorphic rocks in Altyn Tagh directly record the extensive cold subduction along circum-Gondwana after the amalgamation of the main Gondwana blocks, which represents the earliest cold subduction of a global behavior in Earth's history suggesting the emergence of the modern plate tectonics.

Declaration of Competing Interest

The authors declare that they have no known competing financial interests or personal relationships that could have appeared to influence the work reported in this paper.

Acknowledgements

This work was financially supported by a National Natural Science Foundation of China Projects (41730213) and a Grant-in-Aid for Scientific Research from Japan Society for the Promotion of Science (JSPS) to Prof. Toshiaki Tsunogae (18H01300). This work was also supported by a Cross-ministerial Strategic Innovation Promotion Program, entitled "Next-generation technology for ocean resources exploration (Zipangu in the Ocean)" . We are very grateful to Dr. Shan Yu for her great help in the field and Miss Yu Yoneguchi for her assistance in the lab work.

Appendix A. Supplementary data

Supplementary data to this article can be found online at https://doi.org/10.1016/j.gsf.2023.101561.

References

Angel, R.J., Alvaro, M., Miletich, R., Nestola, F., 2017a. A simple and generalised P-T-V EoS for continuous phase transitions, implemented in EosFit and applied to quartz. Contrib. Mineral. Petrol. 172, 1–15.
Angel, R.J., Mazzucchelli, M.L., Alvaro, M., Nestola, F., 2017b. EosFit-Pinc: A simple GUI for host-inclusion elastic thermobarometry. Am. Mineral. 102, 1957–1960.
Angel, R.J., Murri, M., Mihailova, B., Alvaro, M., 2019. Stress, strain and Raman shifts. Z. Kristallogr. Cryst. Mater. 234, 129–140.
Ao, A., Bhowmik, S.K., 2014. Cold subduction of the Neotethys: the metamorphic record from finely banded lawsonite and epidote blueschists and associated metabasalts of the Nagaland Ophiolite Complex. India. J. Metamorph. Geol. 32 (8), 829–860.
Armbruster, T., Bonazzi, P., Akasaka, M., Bermanec, V., Chopin, C., Gieré, R., Heuss-Assbichler, S., Liebscher, A., Menchetti, S., Pan, Y.M., Pasero, M., 2006. Recommended nomenclature of epidote-group minerals. Eur. J. Mineral. 18(5), 551-567.
Ashley, K.T., Caddick, M.J., Steele-MacInnis, M.J., Bodnar, R.J., Dragovic, B., 2014. Geothermobarometric history of subduction recorded by quartz inclusions in garnet. Geochem. Geophy. Geosy. 15(2), 350-360.
Berger, J., Ouzegane, K., Bendaoud, A., Liégeois, J.P., Kiénast, J.R., Bruguier, O., Caby, R., 2014. Continental subduction recorded by Neoproterozoic eclogite and garnet amphibolites from Western Hoggar (Tassendjanet terrane, Tuareg Shield, Algeria). Precambrian Res. 247, 139–158.
Brown, M., Johnson, T., 2018. Secular change in metamorphism and the onset of global plate tectonics. Am. Mineral. 103 (2), 181–196.
Brown, M., Johnson, T., 2019. Metamorphism and the evolution of subduction on Earth. Am. Mineral. 104 (8), 1065–1082.
Brown, M., Kirkland, C.L., Johnson, T.E., 2020. Evolution of geodynamics since the Archean: Significant change at the dawn of the Phanerozoic. Geology 48 (5), 488–492.
Caby, R., Buscail, F., Dembele, D., Diakite, S., Sacko, S., Bal, M., 2008. Neoproterozoic garnet-glaucophanites and eclogites: new insights for subduction metamorphism of the Gourma fold and thrust belt (eastern Mali). Geol. Soc. Spec. Publ. 297 (1), 203–216.
Cao, Y.T., Liu, L., Wang, C., Kang, L., Li, D., Yang, W.Q., Zhu, X.H., 2019a. Timing and nature of the partial melting processes during the exhumation of the garnet–bearing biotite gneiss in the southern Altyn Tagh HP/UHP belt. Western China. J. Asian Earth Sci. 170, 274–293.
Cao, Y.T., Liu, L., Wang, C., Zhang, C., Kang, L., Yang, W.Q., Zhu, X.H., 2019b. Multi-stage metamorphism of the UHP pelitic gneiss from the Southern Altyn Tagh HP/UHP belt, Western China: Petrological and geochronological evidence. J. Earth Sci. 30 (3), 603–620.
Cawood, P.A., Buchan, C., 2007. Linking accretionary orogenesis with supercontinent assembly. Earth Sci. Rev. 82 (3–4), 217–256.
Cawood, P.A., Johnson, M.R., Nemchin, A.A., 2007. Early Palaeozoic orogenesis along the Indian margin of Gondwana: Tectonic response to Gondwana assembly. Earth Planet. Sci. Lett. 255 (1–2), 70–84.
Cawood, P.A., Martin, E.L., Murphy, J.B., Pisarevsky, S.A., 2021. Gondwana's interlinked peripheral orogens. Earth Planet. Sci. Lett. 568, 117057.
Chen, N.S., Sun, M., Wang, Q.Y., Zhang, K.X., Wan, Y.S., Chen, H.H., 2008. U-Pb dating of zircon from the Central Zone of the East Kunlun Orogen and its implications for tectonic evolution. Sci. China Earth Sci. 51 (7), 929–938.
Cheng, H., Zhang, C., Vervoort, J.D., Li, X.H., Li, Q.L., Wu, Y.B., Zheng, S., 2012. Timing of eclogite facies metamorphism in the North Qinling by U-Pb and Lu–Hf geochronology. Lithos 136, 46–59.
Cheng, H., Lu, T.Y., Cao, D.D., 2016. Coupled Lu–Hf and Sm–Nd geochronology constrains blueschist-facies metamorphism and closure timing of the Qilian Ocean in the North Qilian orogen. Gondwana Res. 34, 99–108.
Di Vincenzo, G., Horton, F., Palmeri, R., 2016. Protracted (~ 30 Ma) eclogite-facies metamorphism in northern Victoria Land (Antarctica): Implications for the geodynamics of the Ross/Delamerian Orogen. Gondwana Res. 40, 91–106.
Dong, Y.P., Zhang, G.W., Neubauer, F., Liu, X.M., Genser, J., Hauzenberger, C., 2011. Tectonic evolution of the Qinling orogen, China: review and synthesis. J. Asian Earth Sci. 41 (3), 213–237.
Dong, Y.P., He, D.F., Sun, S.S., Liu, X.M., Zhou, X.H., Zhang, F.F., Yang, Z., Cheng, B., Zhao, G.C., Li, J.H., 2018. Subduction and accretionary tectonics of the East Kunlun orogen, western segment of the Central China Orogenic System. Earth Sci. Rev. 186, 231–261.
Dong, Y.P., Santosh, M., 2016. Tectonic architecture and multiple orogeny of the Qinling Orogenic Belt. Central China. Gondwana Res. 29 (1), 1–40.
Enami, M., Nishiyama, T., Mouri, T., 2007. Laser Raman microspectrometry of metamorphic quartz: A simple method for comparison of metamorphic pressures. Am. Mineral. 92 (8–9), 1303–1315.
Evans, B.W., 1990. Phase relations of epidote-blueschists. Lithos 25 (1–3), 3–23.
Gai, Y.S., Liu, L., Zhang, G.W., Wang, C., Liao, X.Y., Yang, W.Q., Kang, L., Ma, T., Cao, Y. T., 2022. Differential exhumation of ultrahigh-pressure metamorphic terranes: A case study from South Altyn Tagh, western China. Gondwana Res. 104, 236–251.
Ganade de Araujo, C.E., Rubatto, D., Hermann, J., Cordani, U.G., Caby, R., Basei, M.A., 2014. Ediacaran 2,500-km-long synchronous deep continental subduction in the West Gondwana Orogen. Nat. Commun. 5 (1), 1–8.
Gardiner, N.J., Kirkland, C.L., Van Kranendonk, M.J., 2016. The juvenile hafnium isotope signal as a record of supercontinent cycles. Sci. Rep. 6 (1), 1–10.
GBGP (Geological Bureau of Gansu Provincial), 1976. Geological Map of the Subei area, scale 1: 200,000 (in Chinese).
GBGP (Geological Bureau of Gansu Provincial), 1977. Geological Map of the Dangjinshankou and Duobagou areas, scale 1: 200,000 (in Chinese).
GBGP (Geological Bureau of Gansu Provincial), 1979. Geological Map of the Lenghu areas, scale 1: 200,000 (in Chinese).
Ge, R.F., Wilde, S.A., Kemp, A.I.S., Jeon, H.J., Martin, L.A.J., Zhu, W.B., Wu, H.L., 2020. Generation of Eoarchean continental crust from altered mafic rocks derived from a chondritic mantle: The ~3.72 Ga Aktash gneisses, Tarim Craton (NW China). Earth Planet. Sci. Lett. 538, 116225.
Gehrels, G.E., Yin, A., Wang, X.F., 2003. Detrital-zircon geochronology of the northeastern Tibetan plateau. Geol. Soc. Am. Bull. 115 (7), 881–896.
Green, E.C.R., White, R.W., Diener, J.F.A., Powell, R., Holland, T.J.B., Palin, R.M., 2016. Activity–composition relations for the calculation of partial melting equilibria in metabasic rocks. J. Metamorph. Geol. 34, 845–869.
GSIX (Geological Survey Institute of Xinjiang Uygur Autonomous Region), 2009. Geological Map of the Kuoshibulak area, scale 1: 50,000 (in Chinese).
Guynn, J.H., Kapp, P., Gehrels, G., Ding, L., 2012. U-Pb geochronology of basement rocks in central Tibet and paleogeographic implications. J. Asian Earth Sci. 43, 23–50.
Hagen-Peter, G., Cottle, J.M., Smit, M., Cooper, A.F., 2016. Coupled garnet Lu–Hf and monazite U-Pb geochronology constrain early convergent margin dynamics in the Ross orogen. Antarctica. J. Metamorph. Geol. 34 (4), 293–319.
Hames, W.E., Bowring, S.A., 1994. An empirical evaluation of the argon diffusion geometry in muscovite. Earth Planet. Sci. Lett. 124, 161–167.
Han, F.B., Chen, B.L., Cui, L.L., Wang, S.X., Chen, Z.L., Jiang, R.B., Li, L., Qi, W.X., 2012. Zircon SHRIMP U-Pb age of intermediate-acid intrusive rocks in Kaladawan area, eastern Altun Mountains, NW China, and its implications. Acta Petrol. Sin. 28 (7), 2277–2291 (in Chinese with English abstract).
Holder, R.M., Viete, D.R., Brown, M., Johnson, T.E., 2019. Metamorphism and the evolution of plate tectonics. Nature 572 (7769), 378–381.
Holland, T.J.B., Powell, R., 1998. An internally consistent thermodynamic data set for phases of petrological interest. J. Metamorph. Geol. 16 (3), 309–343.
Holland, T., Powell, R., 2003. Activity–composition relations for phases in petrological calculations: An asymmetric multicomponent formulation. Contrib. Mineral. Petrol. 145, 492–501.
Holland, T.J.B., Powell, R., 2011. An improved and extended internally consistent thermodynamic dataset for phases of petrological interest, involving a new equation of state for solids. J. Metamorph. Geol. 29, 333–383.
IGHP (Institute of Geology and Mineral Resource of Henan Province, 1985. Geological Map of the Suoerkuli and Bashikaogong areas, scale 1: 200,000 (in Chinese).
IGQP (Institute of Geology and Mineral Resource of Qinghai Province), 1984. Geological Map of the Mangya area, scale 1: 200,000 (in Chinese).
IGQP (Institute of Geology and Mineral Resource of Qinghai Province), 1986. Geological Map of the Eboliang area, scale 1: 200,000 (in Chinese).
John, T., Schenk, V., 2003. Partial eclogitisation of gabbroic rocks in a late Precambrian subduction zone (Zambia): prograde metamorphism triggered by fluid infiltration. J. Metamorph. Geol. 146 (2), 174–191.
Kawai, T., Windley, B.F., Terabayashi, M., Yamamoto, H., Maruyama, S., Omori, S., Shibuya, T., Sawaki, Y., Isozaki, Y., 2007. Geotectonic framework of the Blueschist Unit on Anglesey-Lleyn, UK, and its role in the development of a Neoproterozoic accretionary orogen. Precambrian Res. 153 (1–2), 11–28.
Leake, B.E., Woolley, A.R., Arps, C.E., Birch, W.D., Gilbert, M.C., Grice, J.D., Hawthorne, F.C., Kato, A., Kisch, H.J., Krivovichev, V.G., Linthout, K., Laird, J., Mandarino, J.,

Maresch, W.V., Nickel, E.H., Rock, N.M.S., Schumacher, J.C., Smith, D.C., Stephenson, N.C.N., Ungaretti, L., Whittaker, E.J.W., Youzhi, G., 1997. Nomenclature of amphiboles; report of the Subcommittee on Amphiboles of the International Mineralogical Association Commission on new minerals and mineral names. Mineral. Mag. 61 (405), 295–310.

Li, J.L., 2020. Blueschist: A window into high-pressure/low-temperature metamorphism and subduction zone dynamics. Sci. China Earth Sci. 63 (12), 1852–1867.

Li, W.Y., Li, S.G., Guo, A.L., Sun, Y.G., Zhang, G.W., 2007. Zircon SHRIMP U-Pb ages and trace element geochemistry of the Kuhai gabbro and the Dur'ngoi diorite in the southern east Kunlun tectonic belt, Qinghai, Western China and their geological implications. Sci. China Earth Sci. 50, 331–338.

Li, X.M., Ma, Z.P., Sun, J.M., Xu, X.Y., Lei, Y.X., Wang, L.S., Duan, X.X., 2009. Characteristics and age study about the Yuemakeqi mafic-ultramafic rock in the southern Altyn Fault. Acta Petrol. Sin. 25 (4), 862–872 (in Chinese with English abstract).

Li, Y.G., Song, S.G., Yang, X.Y., Zhao, Z.F., Dong, J.L., Gao, X.F., Wingate, M.T.D., Wang, C., Li, M., Jin, M.Q., 2020b. Age and composition of Neoproterozoic diabase dykes in North Altyn Tagh, northwest China: implications for Rodinia break-up. Int. Geol. Rev., 1–17

Li, Y.S., Zhang, J.X., Yu, S.Y., Li, S.R., Gong, J.H., 2015. Origin of Early Paleozoic garnet peridotite and associated garnet pyroxenite in the south Altyn Tagh, NW China: constraints from geochemistry, SHRIMP U-Pb zircon dating and Hf isotopes. J. Asian Earth Sci. 100, 60–77.

Li, X.Y., Zhang, C., Behrens, H., Holtz, F., 2020a. Calculating amphibole formula from electron microprobe analysis data using a machine learning method based on principal components regression. Lithos 362, 105469.

Li, Y.S., Zhang, J.X., Yu, S.Y., Li, Y.G., Guo, H., Zhang, J., Fu, C.L., Cao, H., Jin, M.Q., Cai, Z. H., 2020c. Petrological, geochronological, and geochemical potential accounting for continental subduction and exhumation: A case study of felsic granulites from South Altyn Tagh, northwestern China. Geol. Soc. Am. Bull. 132 (11–12), 2611–2630.

Li, S.Z., Zhao, S.J., Liu, X., Cao, H.H., Yu, S., Li, X.Y., Somerville, I., Yu, S.Y., Suo, Y.H., 2018. Closure of the Proto-Tethys Ocean and Early Paleozoic amalgamation of microcontinental blocks in East Asia. Earth Sci. Rev. 186, 37–75.

Liégeois, J.P., Latouche, L., Boughrara, M., Navez, J., Guiraud, M., 2003. The LATEA metacraton (Central Hoggar, Tuareg shield, Algeria): behavior of an old passive margin during the Pan-African orogeny. J. African Earth Sci. 37 (3–4), 161–190.

Linnemann, U., Pereira, F., Jeffries, T.E., Drost, K., Gerdes, A., 2008. The Cadomian Orogeny and the opening of the Rheic Ocean: the diacrony of geotectonic processes constrained by LA-ICP-MS U-Pb zircon dating (Ossa-Morena and Saxo-Thuringian Zones, Iberian and Bohemian Massifs). Tectonophysics 461 (1–4), 21–43.

Liu, Q., Tsunogae, T., Zhao, G.C., Li, J.H., Yao, J.L., Han, Y.G., Wang, P., 2021a. Multiphase ophiolite formation in the Northern Altyn Tagh Orogen, southeastern Tarim. Am. J. Sci. 321 (6), 788–821.

Liu, H., Wang, G.C., Cao, S.Z., Luo, Y.J., Gao, R., Huang, W.X., 2012a. Discovery of Nanhuaian Bimodal volcanics in northern Altyn Tagh and its Tectonic Significance. Earth Sci. J. China Univ. Geosci. 37 (5), 917–928 (in Chinese with English abstract).

Liu, L., Wang, C., Cao, Y.T., Chen, D.L., Kang, L., Yang, W.Q., Zhu, X.H., 2012b. Geochronology of multi-stage metamorphic events: Constraints on episodic zircon growth from the UHP eclogite in the South Altyn, NW China. Lithos 136, 10–26.

Liu, L., Wang, C., Chen, D., Zhang, A., Liou, J.G., 2009. Petrology and geochronology of HP–UHP rocks from the South Altyn Tagh, northwestern China. J. Asian Earth Sci. 35, 232–244.

Liu, C.H., Wu, C.L., Gao, Y.H., Lei, M., Qin, H.P., 2016. Age, composition, and tectonic significance of Palaeozoic granites in the Altyn orogenic belt. China. Int. Geol. Rev. 58 (2), 131–154.

Liu, L., Zhang, A.D., Chen, D.L., Yang, J.X., Luo, J.H., Wang, C., 2007. Implications based on LA-ICP-MS zircon U-Pb ages of eclogite and its country rock from Jianggalesayi area. Altyn Tagh. Earth Sci. Front. 14 (1), 98–107 (in Chinese with English abstract).

Liu, Q., Zhao, G.C., Li, J.H., Yao, J.L., Han, Y.G., Wang, P., Tsunogae, T., 2021b. Provenance of early Paleozoic sedimentary rocks in the Altyn Tagh orogen: Insights into the paleoposition of the Tarim craton in northern Gondwana associated with final closure of the Proto-Tethys Ocean. Geol. Soc. Am. Bull. 133 (3–4), 505–522.

Lu, S.N., Li, H.K., Zhang, C.L., Niu, G., 2008. Geological and geochronological evidence for the Precambrian evolution of the Tarim Craton and surrounding continental fragments. Precambrian Res. 160, 94–107.

Meng, L.T., Chen, B.L., Zhao, N.N., Wu, Y., Zhang, W.G., He, J.T., Wang, B., Han, M.M., 2017. The distribution, geochronology and geochemistry of early Paleozoic granitoid plutons in the North Altun orogenic belt, NW China: Implications for the petrogenesis and tectonic evolution. Lithos 268, 399–417.

Moghadam, H.S., Li, Q.L., Griffin, W.L., Stern, R.J., Santos, J.F., Lucci, F., Beyarslan, M., Ghorbani, G., Ravankhah, A., Tilhac, R., O'Reilly, S.Y., 2021. Prolonged magmatism and growth of the Iran-Anatolia Cadomian continental arc segment in Northern Gondwana. Lithos 384–385, 105940.

Murphy, J.B., Gutierrez-Alonso, G., Nance, R.D., Fernandez-Suarez, J., Keppie, J.D., Quesada, C., Strachan, R.A., Dostal, J., 2006. Origin of the Rheic Ocean: Rifting along a Neoproterozoic suture? Geology 34, 325–328.

Murri, M., Alvaro, M., Angel, R.J., Prencipe, M., Mihailova, B.D., 2019. The effects of non-hydrostatic stress on the structure and properties of alpha-quartz. Phys. Chem. Miner. 46, 487–499.

Nye, J.F., 1957. Physical Properties of Crystals: Their Representation by Tensors and Matrices. Oxford University Press, Oxford.

Palmeri, R., Chmielowski, R., Sandroni, S., Talarico, F., Ricci, C.A., 2009. Petrology of the eclogites from western Tasmania: Insights into the Cambro-Ordovician evolution of the paleo-Pacific margin of Gondwana. Lithos 109 (3–4), 223–239.

Powell, R., Holland, T.J.B., 1988. An internally consistent dataset with uncertainties and correlations: 3. Applications to geobarometry, worked examples and a computer program. J. Metamorph. Geol. 6, 173–204.

Purdy, J.W., Jager, E., 1976. K-Ar ages on rock forming minerals from the central Alps. Institute of Geology and Mineralogy Memoir University of Padova 30, 1–30.

Qi, X.P., Yang, J., Fan, X.G., Cui, J.T., Cai, Z.F., Zeng, X.W., Wei, W., Qu, X.X., Zhai, L.M., 2016. Age, geochemical characteristics and tectonic significance of Changshishan ophiolite in central East Kunlun tectonic melange belt along the east section of East Kunlun Mountains. Geol. China 43, 797–816 (in Chinese with English abstract).

Reno, B.L., Piccoli, P.M., Brown, M., Trouw, R.A.J., 2012. In situ monazite (U–Th)–Pb ages from the Southern Brasília Belt, Brazil: constraints on the high-temperature retrograde evolution of HP granulites. J. Metamorph. Geol. 30 (1), 81–112.

RGGR (Regional Geological Survey Institute of Guangxi Zhuang Autonomous Region), 2002. Geological Map of the Suwushijie area, scale 1: 250,000 (in Chinese).

RGGR (Regional Geological Survey Institute of Guangxi Zhuang Autonomous Region), 2003. Geological Map of the Washixia and Altyn Tagh areas, scale 1: 250,000 (in Chinese).

RGHP (Reginal Geological Survey Institute of Hunan Province), 2003. Geological Map of Aqiang-Qiemo County First Order Station, scale 1: 250,000 (in Chinese).

Romer, T., Mezger, K., Schmädicke, E., 2009. Pan-African eclogite facies metamorphism of ultramafic rocks in the Shackleton Range. Antarctica. J. Metamorph. Geol. 27 (5), 335–347.

Roser, B.P., Korsch, R.J., 1988. Provenance signatures of sandstone-mudstone suites determined using discriminant function analysis of major-element data. Chem. Geol. 67 (1–2), 119–139.

Schmidt, C., Ziemann, M., 2000. In-situ Raman spectroscopy of quartz: A pressure sensor for hydrothermal diamond-anvil cell experiments at elevated temperatures. Am. Mineral. 85, 1725–1734.

Schmitt, R.D.S., Fragoso, R.D.A., Collins, A.S., 2018. Suturing Gondwana in the Cambrian: the orogenic events of the final amalgamation. In: Siegesmund, S., Basei, M., Oyhantcabal, P., Oriolo, S. (Eds.), Geology of Southwest Gondwana, Regional Geology Reviews. Springer, Cham, pp. 411–432.

Schwartz, J.J., Gromet, L.P., Miro, R., 2008. Timing and duration of the calc-alkaline arc of the Pampean Orogeny: implications for the Late Neoproterozoic to Cambrian evolution of Western Gondwana. J. Geol. 116 (1), 39–61.

Sizova, E., Gerya, T., Brown, M., 2014. Contrasting styles of Phanerozoic and Precambrian continental collision. Gondwana Res. 25 (2), 522–545.

Sobolev, S.V., Brown, M., 2019. Surface erosion events controlled the evolution of plate tectonics on Earth. Nature 570 (7759), 52–57.

Song, S.G., Niu, Y.L., Su, L., Xia, X.H., 2013. Tectonics of the north Qilian orogen, NW China. Gondwana Res. 23 (4), 1378–1401.

Steiger, R.H., Jäger, E., 1977. Subcommission on geochronology: convention on the use of decay constants in geo-and cosmochronology. Earth Planet. Sci. Lett. 36 (3), 359–362.

Stern, R.J., 2018. The evolution of plate tectonics. Philos. Trans. Royal Soc. A 376 (2132), 20170406.

Tang, L., Santosh, M., Dong, Y.P., Tsunogae, T., Zhang, S.T., Cao, H.W., 2016. Early Paleozoic tectonic evolution of the North Qinling orogenic belt: evidence from geochemistry, phase equilibrium modeling and geochronology of metamorphosed mafic rocks from the Songshugou ophiolite. Gondwana Res. 30, 48–64.

TIMR (Tianjin Institute of Geology and Mineral Resource), 2007. Geological Map of the Asbestos Ore, scale 1: 250,000 (in Chinese).

Tsujimori, T., Ernst, W.G., 2014. Lawsonite blueschists and lawsonite eclogites as proxies for palaeo-subduction zone processes: A review. J. Metamorph. Geol. 32 (5), 437–454.

Wang, C., 2011. Precambrian tectonic of south margin of Tarim Basin. Ph.D. thesis. Northwest University, 137 pp (in Chinese with English abstract).

Wang, Z., Ji, S., 2001. Elasticity of six polycrystalline silicate garnets at pressure up to 3.0 GPa. Am. Mineral. 86, 1209–1218.

Wang, L.S., Li, Z.M., Yang, P.F., Liu, Y.F., Zhou, N.C., Wei, X.Y., 2016. New evidences for the closure of the Altyn Proto-Tethys Ocean: A case study of high pressure basic granulites from Ring Hills in the Altyn Mountains. Bull. Mineral. Petrol. Geochem. 35 (5), 897–907.

Wang, C., Liu, L., Yang, W.Q., Zhu, X.H., Cao, Y.T., Kang, L., Chen, S.F., Li, R.S., He, S.P., 2013. Provenance and ages of the Altyn Complex in Altyn Tagh: Implications for the early Neoproterozoic evolution of northwestern China. Precambrian Res. 230, 193–208.

Wang, J., Mao, Z., Jiang, F.M., Duffy, T.S., 2015. Elasticity of single-crystal quartz to 10 GPa. Phys. Chem. Miner. 42, 203–212.

Wang, H., Wu, Y.B., Gao, S., Liu, X.C., Gong, H.J., Li, Q.L., Li, X.H., Yuan, H.L., 2011. Eclogite origin and timings in the North Qinling terrane, and their bearing on the amalgamation of the South and North China Blocks. J. Metamorph. Geol. 29 (9), 1019–1031.

Wang, P., Zhao, G.C., Liu, Q., Han, Y.G., Zhang, Y.Y., Yao, J.L., Yu, S., 2021. Slab-controlled progressive evolution of the Kudi back-arc ophiolite in response to the rollback of the Proto-Tethys oceanic slab, in Western Kunlun, NW Tibetan Plateau. Lithos 380, 105877.

Wei, B., 2015. Study on the geological characteristic and tectonic attribute of the ophiolite and island-arc-type igneous rocks, central belt of East Kunlun (eastern section). M.S. thesis, Chang'an University, p. 132 (in Chinese with English abstract).

White, R.W., Powell, R., Holland, T.J.B., Worley, B.A., 2000. The effect of TiO_2 and Fe_2O_3 on metapelitic assemblages at greenschist and amphibolite facies conditions: Mineral equilibria calculations in the system K_2O–FeO–MgO–Al_2O_3–SiO_2–H_2O–TiO_2–Fe_2O_3. J. Metamorph. Geol. 18, 497–511.

White, R.W., Powell, R., Holland, T.J.B., Johnson, T.E., Green, E.C.R., 2014. New mineral activity–composition relations for thermodynamic calculations in metapelitic systems. J. Metamorph. Geol. 32, 261–286.

Whitney, D.L., Evans, B.W., 2010. Abbreviations for names of rock-forming minerals. Am. Mineral. 95, 185–187.

Winkler, H.G.F., 1976. Petrogenesis of Metamorphic Rocks. Springer-Vedag, New York, p. 237.

Wu, Y., 2016. Compositions, Structural Deformation and Geodynamics of the Early Paleozoic Mélange Belt in North Altyn Tagh. Ph.D. thesis, Chinese Academy of Geological Science, p. 193 (in Chinese with English abstract).

XCGS (Xi'an Center of Geological Survey, China Geological Survey), 2012. Geological Map of the Bashikuergan area, scale 1: 250,000 (in Chinese).

Xia, X.H., Song, S.G., Niu, Y.L., 2012. Tholeiite–boninite terrane in the North Qilian suture zone: Implications for subduction initiation and back-arc basin development. Chem. Geol. 328, 259–277.

Xia, B., Zhang, L.F., Du, Z.X., Xu, B., 2019. Petrology and age of Precambrian Aksu blueschist. NW China. Precambrian Res. 326, 295–311.

Yao, J.L., Cawood, P.A., Zhao, G.C., Han, Y.G., Xia, X.P., Liu, Q., Wang, P., 2021. Mariana-type ophiolites constrain the establishment of modern plate tectonic regime during Gondwana assembly. Nature Commun. 12 (1), 1–10.

Yin, J.Y., Xiao, W.J., Sun, M., Chen, W., Yuan, C., Zhang, Y.Y., Wang, T., Du, Q.Y., Wang, X.S., Xia, X.P., 2020. Petrogenesis of Early Cambrian granitoids in the western Kunlun orogenic belt, Northwest Tibet: Insight into early stage subduction of the Proto-Tethys Ocean. Geol. Soc. Am. Bull. 132 (9–10), 2221–2240.

Yoneguchi, Y., Tsunogae, T., Takahashi, K., Sakuwaha, K.G., Ikehata, K., 2021. Pressure-temperature evolution of andalusite-kyanite-sillimanite-bearing pelitic schists from Nishidohira, southern Abukuma Mountains, Northeast Japan: Implications for Cretaceous rapid burial and exhumation in the Northeast Asian continental margin. Lithos 406, 106522.

Yong, W.J., Zhang, L., Hall, C.M., Mukasa, S.B., Essene, E.J., 2013. The $^{40}Ar/^{39}Ar$ and Rb–Sr chronology of the Precambrian Aksu blueschists in western China. J. Asian Earth Sci. 63, 197–205.

Yu, S.Y., Zhang, J.X., del Real, P.G., Zhao, X.L., Hou, K.J., Gong, J.H., Li, Y.S., 2013. The Grenvillian orogeny in the Altun–Qilian–North Qaidam mountain belts of northern Tibet Plateau: Constraints from geochemical and zircon U-Pb age and Hf isotopic study of magmatic rocks. J. Asian Earth Sci. 73, 372–395.

Zhang, Z.C., Guo, Z.J., Song, B., 2009. SHRIMP zircon dating of gabbro from the ophiolite mélange in the northern Altyn Tagh and its geological implications. Acta Petrol. Sin. 25 (3), 568–576 (in Chinese with English abstract).

Zhang, Z.C., Guo, Z.J., Feng, Z.S., Li, J.F., 2010. SHRIMP U-Pb age of zircons from Suoerkuli rhyolite in the Altyn Tagh mountains and its geological significations. Acta Petrol. Sin. 26, 597–606.

Zhang, J.X., Meng, F.C., Yu, S.Y., Chen, W., Chen, S.Y., 2007. ^{39}Ar-^{40}Ar geochronology of high-pressure/low-temperature blueschist and eclogite in the North Altyn Tagh and their tectonic implications. Geol. China 34 (4), 558–564 (in Chinese with English abstract).

Zhang, J.X., Yu, S.Y., Li, Y.S., Yu, X.X., Lin, Y.H., Mao, X.H., 2015. Subduction, accretion and closure of Proto-Tethyan Ocean: Early Paleozoic accretion/collision orogeny in the Altun-Qilian-North Qaidam orogenic system. Acta Petrol. Sin. 31 (12), 3531–3554 (in Chinese with English abstract).

Zhang, J.X., Yu, S.Y., Mattinson, C.G., 2017. Early Paleozoic polyphase metamorphism in northern Tibet, China. Gondwana Res. 41, 267–289.

Zhao, G.C., Wang, Y.J., Huang, B.C., Dong, Y.P., Li, S.Z., Zhang, G.W., Yu, S., 2018. Geological reconstructions of the East Asian blocks: From the breakup of Rodinia to the assembly of Pangea. Earth Sci. Rev. 186, 262–286.